Carbon dots enhance extracellular matrix secretion for dentin-pulp complex regeneration through PI3K/Akt/mTOR pathway-mediated activation of autophagy

Lili Liu [a,b], Xianjing Li [a,b], Wenhuan Bu [c], Nianqiang Jin [c], Yuan Meng [c], Yi Wang [d], Duan Wang [a,b], Xiaowei Xu [a,*], Ding Zhou [a,**], Hongchen Sun [a,***]

[a] *Hospital of Stomatology, Jilin University, Changchun, 130021, PR China*
[b] *Jilin Provincial Key Laboratory of Tooth Development and Bone Remodeling, Jilin University, Changchun, 130021, PR China*
[c] *School and Hospital of Stomatology, China Medical University, Shenyang, 110122, PR China*
[d] *Graduate Program in Applied Physics, Northwestern University, 2145 Sheridan Road, Evanston, IL, 60208, USA*

ARTICLE INFO

ABSTRACT

Pulp injury is one of the most common clinical diseases, and severe cases are usually associated with the functional loss of the tooth, while the current clinical treatment modality is only a cavity filling procedure without the regeneration of the dentin-pulp complex, thus leading to a devitalized and brittle tooth. In this study, carbon dots (CDots) with excellent biocompatibility are prepared from ascorbic acid and polyethyleneimine *via* a hydrothermal method. The as-prepared CDots can enhance extracellular matrix (ECM) secretion of human dental pulp stem cells (DPSCs), giving rise to increased cell adhesion on ECM and a stronger osteogenic/odontogenic differentiation capacity of DPSCs. Further, the mechanism underlying CDots-enhanced ECM secretion is revealed by the transcriptome analysis, Western blot assay and molecular dynamics simulation, identifying that the pharmacological activities of CDots are originated from a reasonable activation of the autophagy, which is mediated by regulating phosphoinositide 3-kinase/protein kinase B/mammalian target of rapamycin signaling pathway. Based on the abundant CDots-induced ECM and thereby the reinforcement of the cell-ECM adhesion, an intact dental pulp stem cell sheet can be achieved, which in return promote *in vivo* the efficient regeneration of dentin-pulp complex as well as blood vessels.

1. Introduction

The damage of dentin-pulp complex caused by caries, pulpitis, pulp necrosis, periapical lesions, and tooth trauma, is a common disease in daily life, which gives rise to unbearable pain, functional loss of the tooth, and eventually loss of quality life [1]. Root canal therapy as a standard of care is utilized in clinical management of this disease, during which all pulp tissues are removed, and then the root canal is enlarged and obturated by the filling materials [2,3]. Nevertheless, this clinical treatment modality is only a cavity filling procedure without the regeneration of the dentin-pulp complex, thus resulting in a devitalized and brittle tooth. Tissue engineering based on stem cells has emerged as an exciting platform for developing therapeutic strategies aimed at the replacement of the damaged tissues and thereby the repair of the physiological function [4–6]. Recent studies have demonstrated that human dental pulp stem cells (DPSCs) have been successfully engineered to regenerate the dentin-pulp complex, where a scaffold is usually required to load the DPSCs to decrease the loss of DPSCs compared to isolated stem cell suspensions [7–9]. Yet most scaffolds are exogenous and suffer from potential immune rejection [10]. As a natural, multifunctional and endogenous scaffold, extracellular matrix (ECM) secreted by DPSCs can store growth factors, promote cellular differentiation, regulate intercellular communication, and particularly provide structural and biochemical support to surrounding cells [11]. Further, ECM could promote cell adhesion on ECM and makes it possible to develop DPSCs-based cell sheet engineering for the dentin-pulp complex regeneration without

immune rejection [12,13]. However, owing to the limited production of ECM, the DPSCs show a low viability and the resultant cell sheet is usually fragile or broken, leading to an inefficient regeneration of the dentin-pulp complex [14]. Consequently, it is significant to explore an effective way to enhance the ECM secretion of DPSCs for improving the structural integrity of the cell sheet and further promoting the dentin-pulp complex regeneration.

Currently, one strategy to promote the ECM secretion is to utilize growth factors [15–17], while the extraction processes are quite complex and the products are hard to be preserved for a long time at room temperature, thus resulting in a high cost and a limited application [18]. Besides, ascorbic acid as a reductant can induce the synthesis of collagen (one of the major components of ECM) through reducing Fe^{3+} to Fe^{2+} and ensuring the hydroxylase reaction cycle, but the easy oxidizability of ascorbic acid causes concern about their long-term stability in storage [19]. Nanomaterials have gained increasing attention in biology owing to their distinct advantages, including facile preparation [20], low cost [21], long-term preservation [22], abundant surface groups [23], and so forth [24–26]. Several kinds of nanomaterials, such as Ag nanoparticle [27], TiO_2 nanotube [28], and carbon nanotube [29–31], have been demonstrated to be capable of increasing the collagen secretion in non-stem cells, whereas there are few studies about their applications in stem cells. More importantly, although collagen plays a key role in cell-ECM adhesion, another two components of ECM (namely, fibronectin and integrin) are needed as well, since the establishment of the cell-ECM connections is *via* the binding of fibronectin to collagen and cell-surface integrin [11]. With excellent biocompatibility, strong fluorescence properties, and nanoscale size, carbon dots (CDots) as an emerging class of carbon-based nanomaterials have great potential in various biomedical applications, including anti-inflammation [32], bacteriostasis [33], bioimaging [34] and so on [35,36]. A majority of CDots are usually prepared from the organic precursors with carbonyl and amine groups through amidation reaction similar to the formation of peptide bond in protein. Thus some CDots share similar properties as biomacromolecule, such as enzyme [37,38]. Therefore, these accomplishments inspire us to develop a novel CDots-based medicine to address the challenges of promoting the ECM secretion of DPSCs and the
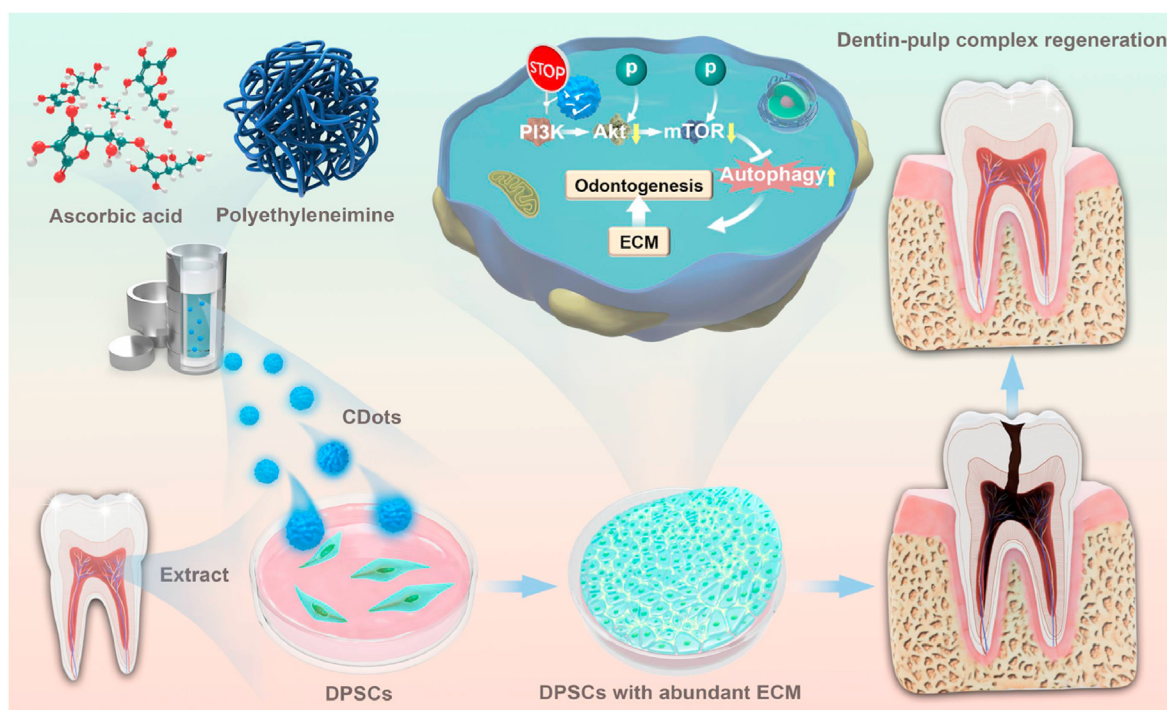
dentin-pulp complex regeneration thereof.

In this study, we reported the synthesis of a blue photoluminescent CDots with excellent biocompatibility through one-step hydrothermal treatment of ascorbic acid and polyethyleneimine (PEI), and offered an approach to regenerate the dentin-pulp complex, which is hardly achieved by other CDots that have been reported. The as-prepared CDots were characterized by abundant functional groups along with a large π-conjugated structure, and could induce a reasonable activation of the autophagy of DPSCs through phosphoinositide 3-kinase (PI3K)/protein kinase B (Akt)/mammalian target of rapamycin (mTOR) signaling pathway, which was confirmed by transcriptome analysis, Western blot assay and molecular dynamics simulation. As a result, DPSCs treated by CDots could secret more ECM-related proteins, including fibronectin, integrin β1 and collagen type I (COL1), leading to the cell-ECM adhesion reinforcement, and a stronger osteogenic/odontogenic differentiation capacity of DPSCs, all of which promoted *in vivo* the efficient regeneration of dentin-pulp complex as well as blood vessels (Scheme 1).

2. Materials and methods

2.1. Materials

Ascorbic acid (99.99%) and polyethyleneimine (PEI, MWCO = 1800 D, 99%) were purchased from Macklin (Shanghai, China) and Aladdin Ltd (Shanghai, China), respectively. Dulbecco's modified Eagle medium (DMEM) with high glucose and penicillin-streptomycin were purchased from Hyclone (Logan, UT, USA). Fetal bovine serum was obtained from Biological Industries (Cromwell, CT, USA). Cell counting kit-8 (CCK-8) was purchased from Apexbio Technology LLC (Houston, TX, USA). Cell cycle and Annexin V-APC apoptosis analysis kit were obtained from Sungene Biotech (Tianjin, China). RNeasy mini purification kit was purchased from Qiagen (Valencia, CA, USA), PrimeScript RT Master Mix and SYBR Premix Ex Taq were from TaKaRa (Dalian, China). Protease/ phosphatase inhibitor cocktail was obtained from MedChenExpress LLC (Monmouth Junction, NJ, USA). Radioimmunoprecipitation assay (RIPA) buffer, 4,6-diamidino-2-phenylindole (DAPI), sodium dodecyl sulfate polyacrylamide gel electrophoresis (SDS-PAGE), and bovine serum

Scheme 1. Schematic illustration of the synthetic procedure of CDots and the working mechanism for promoting dentin-pulp complex regeneration.

albumin (BSA) were purchased from Beyotime (Shanghai, China). Secondary antibodies and Cy3-labeled IgG antibody were from Proteintech (Rosement, IL, USA). Ascorbic acid, β-glycerophosphate disodium salt hydrate, alizarin red S (ARS), alkaline phosphatase (ALP) staining kit, dexamethasone, indomethacin, insulin, 3-isobutyl-1-methylxanthine and Oil Red O were purchased from Sigma Aldrich Co. (St Louis, MO, USA). Spautin-1 was purchased from Selleckchem (Houston, TX, USA). SC79 and 740Y–P were obtained from MCE (Monmouth Junction, NJ, USA).

2.2. Synthesis and characterization of carbon dots (CDots)

In this study, CDots were synthesized according to the following procedures. First, 1 g of ascorbic acid and 0.5 g of PEI were dissolved in 15 mL of deionized water. The clear solution was transferred into a 20 mL Teflon-lined stainless-steel autoclave and placed into an oven heated at 200 °C. After 8 h, the autoclave was cooled to room temperature and the CDots aqueous solution was obtained. Afterwards, to purify the CDots, the as-prepared CDots solution was dialyzed in deionized water using a dialysis bag (MWCO of 1000) for 48 h to remove large particles including unreactive PEI and other agglomerated particles. Then, the vacuum rotary evaporator was used to concentrate the dialysate outside dialysis bag by the evaporation of water. The concentrated sample was further dialyzed in deionized water using a dialysis bag (MWCO of 100–500) for 24 h to remove small molecular reagents. Next, the purified CDots solution was condensed and free-dried. Finally, The CDots were redissolved in deionized water for the following experiments.

For the characterization of the CDots, ultraviolet–visible (UV–vis) absorption spectra were collected using a Lambda 800 UV–vis spectrophotometer. Photoluminescence (PL) spectroscopy was acquired using a Shimadzu RF-5301 PC spectrophotometer. To obtain the images of high-resolution transmission electron microscopy, the CDots solution was dropped on the micro grid copper mesh, dired in the oven, and the as-prepared sample was then observed with a Hitachi H-800 electron microscope at an acceleration voltage of 200 kV with a CCD camera. Zeta potential of the CDots was analyzed by dynamic light scattering (DLS) (Zetasizer NanoZS, Malvern Instruments, Britain) at a neutral pH and room temperature. Energy-dispersive spectra (EDS) was performed with the help of Inca X-Max instrument (Oxford Instruments). For detecting functional groups in the CDots, Fourier transform infrared (FTIR) spectra were implemented by a Nicolet AVATAR 360 FTIR instrument. For measuring the elemental composition of the CDots, the CDots solution was dropped on the silicon wafer, and then the sample was dried at room temperature. X-ray photoelectron spectroscopy (XPS) was conducted using a VG ESCALAB MKII spectrometer with a Mg KR excitation (1253.6 eV). Binding energy calibration was based on C 1s at 284.6 eV.

2.3. In vitro cell culture, cytotoxicity assays and cell imaging

All procedures were approved by the Medical Ethics Committee of Stomatological Hospital of Jilin University (approval number: 202045), and all samples were collected with informed consents. Human dental pulp stem cells (DPSCs) were isolated from adult third molars and incubated in DMEM with high glucose containing 10% FBS, 100 U/mL of penicillin and 100 μg/mL of streptomycin. DPSCs were cultured in a humidified environment at 37 °C under 5% CO_2 and culture medium was replaced every 2–3 days. DPSCs at passages 3–4 were used for this study.

The multiple differentiation capacity of DPSCs was identified by alizarin red S (ARS) and Oil Red O staining. DPSCs were seeded into 6-well plates at a density of 1×10^5 cells/well and cultured overnight. Culture medium was replaced with osteogenic induction medium, containing 50 μg/mL of ascorbic acid and 10 mmol/L of β-glycerophosphate for 21 days. The cells were fixed with 4% paraformaldehyde for 30 min and then stained with ARS for 15 min. Then the general photograph of ARS staining was obtained by a scanner and the red nodules were observed under an inverted microscope. For adipogenic induction, culture medium was replaced with adipogenic induction solution,

containing 2 μM of dexamethasone, 0.2 mM of indomethacin, 0.01 mg/mL of insulin and 0.5 mM of 3-isobutyl-1-methylxanthine. The medium was changed every 3 days, after which the induction and fixation steps were performed, and 0.3% Oil Red O (Cyagen Biosciences) staining was used for 30 min at room temperature. The adipogenic droplets were then observed under an inverted microscope. The phenotype of DPSCs was identified by flow cytometry (FCM, BD Biosciences, San Jose, CA, USA) using CD44 (Biolegend, San Diego, CA, USA), CD90 (Biolegend) and CD105 (Biolegend) as positive surface markers, CD3 (Biolegend), CD45 (Biolegend), CD14 (Proteintech) and CD 34 (Proteintech) as negative surface markers.

In vitro cytotoxicity of CDots was assessed by CCK-8, cell cycle and apoptosis assays. DPSCs were seeded at 5×10^3 cells/well in a 96-well plate and cultured overnight. Culture medium was replaced with 200 μL of medium containing different concentrations of CDots at 0, 20, 50, 100, 200, or 300 μg/mL, respectively. After 24 h of incubation, the medium was removed, and 100 μL of medium containing 10 μL of CCK-8 reagent was added into each well. After 30 min of incubation, the absorbance was measured at 450 nm using a microplate reader (RT-6000; Rayto Life and Analytical Science Co, Shenzhen, China). Percentage of cell viability was calculated compared to the control group. DPSCs were seeded in a 6-well plate and cultured overnight. Culture medium was replaced with 2 mL of medium containing CDots at 0, 20, 50, 100, or 200 μg/mL, respectively. After 24 h of incubation, cells were collected, washed twice with cold PBS. Subsequently, for cell cycle assay, cells were stained by PI/RNase staining solution. For cell apoptosis assay, cells were resuspended by 100 μL of binding buffer and stained using 5 μL of Annexin-V-FITC and 5 μL of 7-AAD working solution according to the manufacturer's instructions. Finally, these stained cells were analyzed with flow cytometry in 1 h.

DPSCs were seeded at 1×10^5 cells/well in a 6-well plate and cultured overnight. Then, culture medium was replaced with 2 mL of medium containing CDots at 200 μg/mL. After 4 h of incubation, the cells were fixed in 4% paraformaldehyde for 10 min at room temperature, washed twice with PBS and observed by confocal laser scanning microscopy (CLSM, Olympus, Japan).

2.4. Western blot analysis

DPSCs were seeded at 1×10^6 cells/dish in 10 cm cell culture dishes and cultured overnight. Then the culture medium was replaced with 10 mL of medium containing CDots at 0, 50, 100 and 200 μg/mL. Cells were washed twice with PBS and lysed in RIPA buffer containing protease and phosphatase inhibitor. Then proteins were quantified using a BCA protein assay. Subsequently, 30 μg of protein from each group was separated by 10% SDS-PAGE and then transferred to a polyvinylidene fluoride (PVDF) membrane. The membrane was first incubated in 5% BSA for 1 h at room temperature for blocking nonspecific binding sites and then incubated with the following primary antibodies overnight at 4 °C: anti-GAPDH (10494-1-AP, 1:2000 (Proteintech)), anti-fibronectin (15613-1-AP, 1:1000 (Proteintech)), anti-integrin β1 (26918-1-AP, 1:1000 (Proteintech)), anti-collagen type I (14695-1-AP, 1:1000 (Proteintech)), anti-E-cadherin (20874-1-AP, 1:1000 (Proteintech)), anti-DSPP (SC-73632, 1:100 (Santa Cruz)), anti-DMP1 (SC-73633, 1:100 (Santa Cruz)), anti-BSP (SC-73630, 1:100 (Santa Cruz)), anti-LC3B (18725-1-AP, 1:1000 (Proteintech)), anti-P62 (18420-1-AP, 1:1000 (Proteintech)), anti-Beclin1 (11306-1-AP, 1:1000 (Proteintech)), anti-p-Akt (9271S, 1:1000 (CST)), anti-Akt (9272S, 1:1000 (CST)), anti-p-mTOR (67778-1-Ig, 1:1000 (Proteintech)) and anti-mTOR (66888-1-Ig, 1:1000 (Proteintech)). The following day, the membrane was incubated with the secondary antibodies at room temperature for 1 h. Finally, enhanced chemiluminescence reagent was used to visualize the protein bands and ImageJ software was used to analyze the band density. To further evaluate the role of autophagy, Akt and PI3K in CDots-enhanced secretion of ECM, spautin-1, SC79 and 740Y–P were added and the same procedure was used.

2.5. Reverse transcriptase quantitative polymerase chain reaction (RT-qPCR)

DPSCs were cultured in 6-well plates with 2 mL of medium containing CDots at 0 and 200 μg/mL for 3, 7, 10 and 14 days. Total RNA was extracted using an RNeasy mini purification kit, and cDNAs were synthesized using iScript cDNA synthesis kit. The RT-qPCR assays were conducted using SYBR Premix Ex Taq and MxPro Mx3005P real-time PCR detection system (Agilent Technologies, Santa Clara, CA). Primer sequences are listed in Table S1. ACTB was used as an internal control.

2.6. Immunofluorescence staining

DPSCs were seeded on coverslips at 1×10^4 cells/well in a 6-well plate and cultured overnight. Then the medium was replaced with 2 mL medium containing CDots at 0 and 200 μg/mL. After 24 h of incubation, the cells were fixed by 4% paraformaldehyde for 20 min and permeabilized with 0.2% Triton X-100 for 5 min at room temperature. 5% BSA was used to block nonspecific binding sites for 1 h at room temperature. Then, the cells were incubated with fibronectin antibody (15613-1-AP, 1:500 (Proteintech)), collagen type I antibody (14695-1-AP, 1:500 (Proteintech)) and integrin β1 antibody (26918-1-AP, 1:500 (Proteintech)) at 4 °C overnight. The following day, the cells were incubated with Cy3-labeled secondary antibody at room temperature for 1 h in the dark. Finally, the cells were treated with DAPI for 5 min and captured by an inverted fluorescence microscope.

2.7. Alkaline phosphatase staining

DPSCs were seeded into 6-well plates at a density of 1×10^5 cells/well and cultured overnight. Culture medium was replaced with osteogenic induction medium, containing 50 μg/mL of ascorbic acid and 10 mmol/L of β-glycerophosphate for 7 days and 14 days. Then, cells were fixed in 4% paraformaldehyde for 15 min at room temperature and incubated with the ALP staining kit following the manufacturer's instruction. The stained cells were observed and imaged using an inverted microscope.

2.8. Fabrication and observation of dental pulp stem cell sheets

DPSCs were seeded at 1×10^6 cells/dish in 10 cm cell culture dishes and cultured overnight in an incubator that is dark environment. Then the culture medium was replaced with 10 mL of medium containing CDots at 200 μg/mL. After an additional 10 days of culture, dental pulp stem cell sheet was harvested. Then, the cell sheet of each group was observed by an inverted fluorescence microscope to confirm the CDots imaging in the cell sheet. Finally, the cell sheet was fixed by 4% paraformaldehyde and underwent dehydration, paraffin-embedding, sectioning, and hematoxylin and eosin (H&E) staining. The structure of the cell sheet was observed by microscope.

2.9. Transmission electron microscope (TEM)

DPSCs were seeded at 1×10^6 cells/dish in 10 cm cell culture dishes and cultured overnight. Then the culture medium was replaced with 10 mL of medium containing CDots at 0 and 200 μg/mL. After 24 h of incubation, cells were harvested and fixed in 4% glutaraldehyde for 4 h, dehydrated with graded ethanol and embedded in epon. Ultrathin sections were stained with citrate and uranyl acetate and observed using TEM (TECNAI SPIRIT, FEI Company, Czech Republic).

2.10. Transcriptome analysis by RNA sequencing

Total RNA was extracted using the TRIzol reagent according to the manufacturer's protocol. RNA purity and quantification were measured using the NanoDrop 2000 spectrophotometer (Thermo Scientific, USA).

RNA integrity was evaluated using the Agilent 2100 Bioanalyzer (Agilent Technologies, Santa Clara, CA, USA). Then the libraries were constructed using TruSeq Stranded mRNA LT Sample Prep Kit (Illumina, San Diego, CA, USA) according to the manufacturer's instructions. The transcriptome sequencing and analysis were conducted by OE Biotech Co., Ltd. (Shanghai, China). mRNA and RNA sequencing were performed to investigate the global expression profile of DPSCs and CDots-treated DPSCs (n = 3), and 150 bp paired-end reads were generated. Raw data (raw reads) of fastq format were firstly processed using Trimmomatic and the low quality reads were trimmed to obtain the clean reads. Then the clean reads were mapped to the human genome (GRCh38) using HISAT2. FPKM of each gene was calculated using Cufflinks, and the read counts of each gene were obtained by HTSeq-count. Differential expression analysis was obtained using the DESeq (2012) R package. P value < 0.05 and foldchange >2 or foldchange <0.5 was set as the threshold for significantly differential expression. Hierarchical cluster analysis of differentially expressed genes (DEGs) was performed to demonstrate the expression pattern of genes in different groups and samples. GO enrichment and KEGG pathway enrichment analysis of DEGs were conducted respectively using R based on the hypergeometric distribution.

2.11. Homology modeling and molecular dynamics (MD) simulations

The homology modeling was performed *via* MODELLER package, where the whole FASTA sequence of PI3K (*i.e.*, p110α and p85α) were retrieved from RCSB Protein Data Bank (PDB; the PDB ID is4ovu), and the structures from PDB entry 4ovu were selected as the overall chain templates. The resultant homology models were evaluated by Ramachandran plot analysis. The simplified model of CDots was proposed based on the HRTEM and XPS analysis and optimized by using density functional theory method as carried out in the Gaussian09 software package. The 6-31G* basis set was selected to combine with the functional B3LYP throughout all calculations (B3LYP/6-31G*). All the structures were visualized by the Visual Molecular Dynamics (VMD) program.

The MD simulation was carried out utilizing the GROMACS package version 2018.8 under AMBER99SB-ILDNP force field for all-atom simulations. Transferable intermolecular interaction potential 3 points (TIP3P) water molecules were used to solvate the system in a cubic box with a minimum distance of 10 Å between the protein and the edge of the box. The extra charges of the system were neutralized with Na^+ ions. Periodic boundary conditions were used in all directions to mimic the infinite system. Steepest descents and/or conjugate gradient minimization (with a tolerance of up to 1000 kJ/mol/nm) were made to eliminate any adverse interaction. Before the production simulation, a two-step equilibration was made. During these two stages, all atoms of the system were restrained in position to prevent any conformational change. The systems were first simulated under a constant volume (NVT) ensemble to achieve 300 K by the V-rescale method for 1 ns? Then, the equilibrated structures from the NVT ensemble were subjected to constant pressure (NPT) equilibration (1 ns) using the Parrinello-Rahman barostat under an isotropic pressure of 1.0 bar. Production MD was conducted for 120 ns without any restraints. The trajectories from the simulations were saved for every 10 ps for analysis of root mean square deviation (RMSD), root mean square fluctuation (RMSF) as well as the protein-ligand contacts. The binding energy was calculated by the molecular mechanics Poisson-Boltzmann accessible surface area (MM-PBSA) method.

2.12. Fabrication of human treated dentine matrix fragments (hTDMFs) and dentin-pulp complex regeneration in vivo

Briefly, the premolar teeth were collected and periodontal ligament tissues were removed mechanically. Then, outer cementum, inner dental pulp, predentin and partial root dentin were also ground carefully. The hTDMFs were cut into 5–7 mm sections and the root space was formed to

a diameter of 2–4 mm. Next, the hTDMFs were soaked in deionized water for 5 h and meanwhile concussed using an ultrasonic cleaner for 20 min each hour. The deionized water was changed once every hour. Then, the hTDMFs were first soaked in 17% ethylenediamine tetraacetic acid (EDTA) for 5 min, washed in deionized water for 10 min, then exposed to 5% EDTA for 10 min and washed in deionized water for 10 min. The hTDMFs were exposed to sterile PBS with 100 units/mL of penicillin and 100 μg/mL of streptomycin for 3 days, then washed in sterile deionized water for 10 min. Finally, the hTDMFs were stored in DMEM at 4 °C.

All animal procedures were performed in accordance with animal care guidelines approved by the Animal Ethics Committee of No. 1 Hospital of Jilin University (approval number: 20200470). Cell sheets in each group were put into the cavity of hTDMFs and then the grafts were transplanted into subcutaneous space at the back of 6 weeks old male BALB/c nude mice. Fifteen weeks later, the mice were euthanized and all samples were harvested for histological analysis. All the animal experiments were conducted in accordance with the committee guidelines of Jilin University for animal experiments. All implants were fixed in 4%
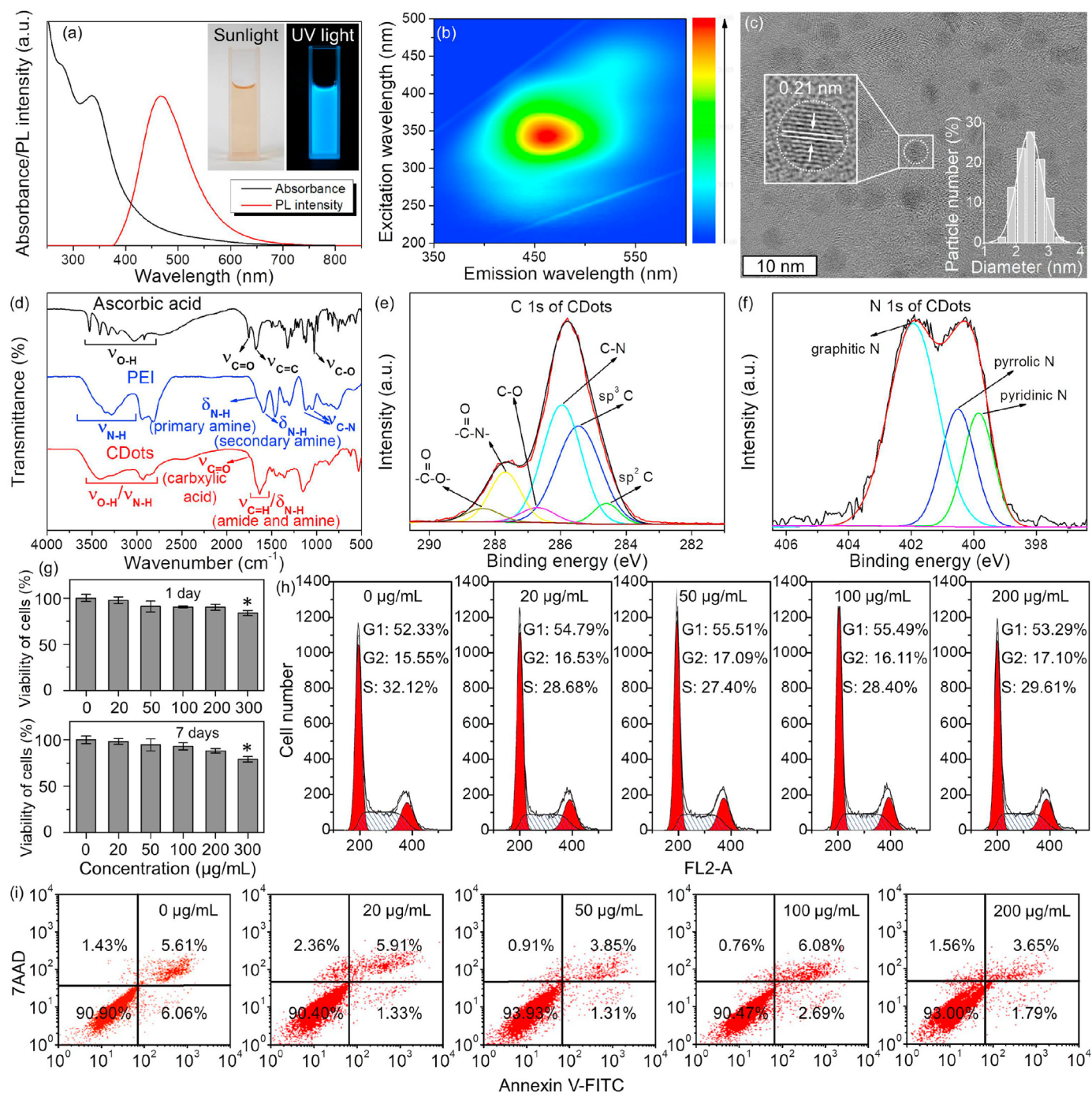

Fig. 1. Characterizations and cytotoxicity assays of CDots. (a) UV–vis absorption (black) and PL emission spectra (red) of CDots. Insets: photographs of CDots solution taken under sunlight (left) and UV light (right), respectively. (b) Excitation-emission map of CDots. (c) HRTEM image of CDots. (d) FTIR spectra of ascorbic acid (black), PEI (blue), and CDots (red). (e–f) High-resolution XPS spectra of CDots: (e) C 1s and (f) N 1s. (g) CCK-8 assay of DPSCs treated with CDots at different concentrations of 20, 50, 100, 200, and 300 μg/mL on day 1 and 7, respectively. Data are presented as mean ± SD from three independent experiments. * indicates $P < 0.05$ *vs.* vehicle. (h) Cell cycle assay and (i) apoptosis assay of DPSCs treated with CDots at different concentrations of 20, 50, 100, and 200 μg/mL, respectively. (For interpretation of the references to colour in this figure legend, the reader is referred to the Web version of this article.)

paraformaldehyde overnight at 4 °C, decalcified with 10% EDTA, embedded in paraffin, and cut into 5 μm sections. Finally, deparaffinized sections were stained with H&E. Immunohistochemical antibodies included DSPP antibody (SC-73632, 1:100 (Santa Cruz)), DMP1 antibody (SC-73633, 1:100 (Santa Cruz)) and CD31 antibody (ARG52748, 1:50 (arigobio)).

2.13. Statistical analysis

Each experiment was repeated at least three times. All measurements were presented as the mean ± standard deviation. Statistical analyses were performed by one-way ANOVA. A value of $P < 0.05$ was considered statistically significant.

3. Results and discussion

3.1. Synthesis and characterization of CDots

In this study, CDots were synthesized *via* a one-pot hydrothermal treatment of ascorbic acid and PEI. Afterwards, the as-prepared CDots solution was dialyzed in deionized water using a dialysis bag (MWCO of 1000) for 48 h to remove large particles including unreactive PEI and other agglomerated particles. The aqueous solution outside the dialysis membrane, which is mainly composed of CDots and other small molecular reagents, was further dialyzed in deionized water using a dialysis bag (MWCO of 100–500) for 24 h to remove small molecular reagents. Thus, these dialysis processes ensure the purity of the CDots solution [33], and the purified CDots solution presented yellow color under sunlight, while under ultraviolet (UV) light a bright blue photoluminescence (PL) emission could be observed. Fig. 1a showed the UV–vis absorption spectrum of the CDots solution, which was obviously different from those of the raw material (Fig. S1), indicating the formation of CDots after the hydrothermal treatment, which was also confirmed by the variations of their PL spectra (Fig. 1a and S1). The PL spectrum of the CDots solution exhibited a peak located at 460 nm at an excitation wavelength of 350 nm, while both ascorbic acid and PEI had no PL emission under UV light (Fig. S1a and b). Additionally, the excitation-emission map of the CDots solution presented a single emission centered at 460 nm (Fig. 1b), suggesting the size uniformity and providing an efficient way to examine the behaviors of CDots in biological systems therewith. To elucidate their morphology, high-resolution transmission electron microscopy (HRTEM) was used to characterize the morphology and structure of CDots. As shown in Fig. 1c, CDots possessed a uniform size with an average diameter of 2.5 nm, which was beneficial to enter into the cell and thereby exert the pharmacological function of CDots. The well-resolved lattice spacing of 0.21 nm conforms to the (100) crystallographic facets of graphitic carbon [39], indicating the formation of a graphene-like structure. Besides, the zeta potential of CDots in aqueous solution was measured to be 15.7 mV (Fig. S2). This positive potential is mainly due to the presence of plentiful amine groups in CDots originated from PEI, which can be confirmed by the following characterizations, and this positive value also facilitates the entry of CDots into cells, since the cell membrane usually possesses a negative potential [40]. Energy dispersive spectrum (EDS) demonstrated the existence of C, N and O elements in CDots (Fig. S3). All of O and a portion of C were from ascorbic acid, whereas PEI provided all of N and the other portion of C. To further account for the chemical structure of CDots, Fourier transform infrared (FTIR) and X-ray photoelectron spectroscopy (XPS) characterizations were conducted.

As presented in Fig. 1d, the FTIR spectrum of ascorbic acid presented a C–O stretching vibration located at 1027 cm^{-1}, a C=O stretching vibration at 1753 cm^{-1}, and an O–H stretching vibration at 2916-3525 cm^{-1}, suggesting the existence of carboxyl and hydroxyl groups. The FTIR spectrum of PEI exhibited two C–N stretching vibrations at 1120 and 1057 cm^{-1} as well as two N–H bending vibrations located at 1662 and 1593 cm^{-1}, constituting the primary and secondary amines,

respectively. The amine groups of PEI and the carboxyl/hydroxyl groups of ascorbic acid ensure the subsequent dehydration condensation and carbonization to form the CDots [39,41]. In the FTIR spectrum of the CDots, an O–H/N–H stretching vibration ranging from 2800 to 3600 cm^{-1} and a C=O stretching vibration at 1720 cm^{-1} indicates the existence of the carboxyl and amine groups in CDots (Fig. 1d). Additionally, a relatively broad band displayed at 1592 cm^{-1}, covering C=O stretching vibration (*i.e.*, amide I band), N–H bending vibration (*i.e.*, amide II band), and N–H bending vibration of free amine groups, resulting in the overlap of the amide I and II band. These results verify that the formation of CDots is because of dehydration condensation and further carbonization between the carboxyl/hydroxyl and amine groups, and abundant functional groups are located in CDots, which could be further proved by the following XPS characterizations. In Fig. S4a, the C 1s spectrum of ascorbic acid showed four peaks at 284.7, 285.7, 286.6 and 288.4 eV, indicating the presence of sp^2 C, sp^3 C, C–O and –COO–, respectively. The N 1s spectrum of PEI showed one peak centered at 399.9 eV (Fig. S4b), which was associated with the amine group (–NH–). In comparison, the C 1s spectrum of the CDots could be fitted with six peaks at 284.6, 285.4, 285.9, 286.7, 287.7 and 288.3 eV (Fig. 1e), belonging to sp^2 C, sp^3 C, C–N, C–O, –CON– and –COO–, respectively. The existence of –CON– is attributed to the amidation reaction between ascorbic acid and PEI, and the species of sp^2 C demonstrate a highly conjugated sp^2 domain in CDots, which is in accordance with the result of the HRTEM (*i.e.*, a graphene-like structure) (Fig. 1c). In addition, the N 1s spectrum of CDots exhibited three peaks at 399.3, 400.5 and 401.9 eV (Fig. 1f), which were assigned to pyridinic N, pyrrolic N, and graphitic N, respectively, representing the presence of heterocyclic groups. The XPS characterizations further reveal the formation process of CDots and the existence of abundant functional groups in CDots, which provide great potential for further use in biological applications.

3.2. In vitro characterization of DPSCs and biocompatibility of CDots with DPSCs

The primary DPSCs were isolated from adult third molars (Fig. S5) and incubated for 14 days, after which the purified DPSCs could be acquired through two trypsinization passages. Fig. S6a showed that the cells possessed a fibroblastic and spindle-like shape in accordance with the morphology of mesenchymal stem cells. Since these cells are originated from dental pulp, it can be safely concluded that the isolated cells should be DPSCs. To further clarify this conclusion, the multi-differentiation capacity of the cells was examined by alizarin red S (ARS) and Oil Red O staining assays. After being incubated in osteoinduction medium for 21 days and stained by ARS, lots of red mineralized nodules could be observed (Fig. S6b), indicating the osteogenic differentiation. Besides, following 28 days of adipogenic induction, several beaded adipogenic droplets were found in the cytoplasm and could be specifically stained in red with the Oil Red O (Fig. S6c), suggesting the adipogenic differentiation. According to these results, the isolated cells with multi-differentiation capacity could be identified as DPSCs. Flow cytometry analysis was also carried out to characterize the isolated DPSCs. Fig. S6d showed that the DPSCs could be stained positively for mesenchymal stem cell marker CD44, extracellular matrix protein CD90, and adhesion molecule CD105, but negatively for hematopoietic cell markers CD3, CD45, CD14 and CD34, thus indicating a typical pattern of mesenchymal stem cells, namely, the successful isolation of the DPSCs.

The biocompatibility of CDots with DPSCs, as a prerequisite for their further *in vivo* and *in vitro* studies, should be evaluated. Using cell counting kit-8 (CCK-8) assay, CDots were found to have no effects on the proliferation of DPSCs as increasing the dose of CDots from 0 to 200 μg/mL, whereas the viability decreased to 83% and 79% at 300 μg/mL of CDots on day 1 and 7, respectively (Fig. 1g). Then we concluded that the appropriate concentration of CDots was 200 μg/mL. Apart from CCK-8 assay, flow cytometry analysis was performed to examine the effects of CDots on the apoptosis of DPSCs (Fig. 1i and Fig. S7a). The result reveals

that the apoptosis of DPSCs appears no significant difference after treatment by CDots with concentrations ranging from 0 to 200 μg/mL. Moreover, the cell cycle of DPSCs treated by CDots was also investigated by flow cytometry. Fig. 1h and Fig. S7b showed that the proportion of DPSCs in the S phase, as a crucial indicator in DNA duplication of the cell cycle, were nearly unchanged when treated by CDots from 0 to 200 μg/mL, demonstrating the excellent biocompatibility of CDots. Furthermore, the blue PL emission of CDots can be utilized for tracing the distribution of CDots, and therewith clarifying their function, which is seldom achieved by other conventional drugs. After the co-incubation with CDots for 24 h, the DPSCs presented a blue fluorescence (Fig. 2a), proving that the blue photoluminescent CDots could be internalized into the cells and mainly distributed in the cytoplasm. The internalization of CDots lays the foundation for the exertion of their pharmacological function.

Interestingly, in the experiments, the DPSCs treated by CDots were easier to be scraped from the culture dish with cell-cell connections than those without CDots treatment, implying a stronger adhesion among these cells, which was closely associated with the amount of ECM.

3.3. CDots-promoted ECM secretion and the associated effects on DPSCs

To investigate the effects of CDots on ECM secretion, DPSCs were cultured and treated by CDots at different concentrations (50, 100 and 200 μg/mL) for 7 days, and then Western blot assay was performed. As seen in Fig. 2b and c, the expressions of fibronectin, integrin β1, and COL1, as the representative ECM-related proteins, appeared an obvious upregulation as increasing the concentration of CDots from 0, 50, 100–200 μg/mL, suggesting that CDots can promote ECM production of
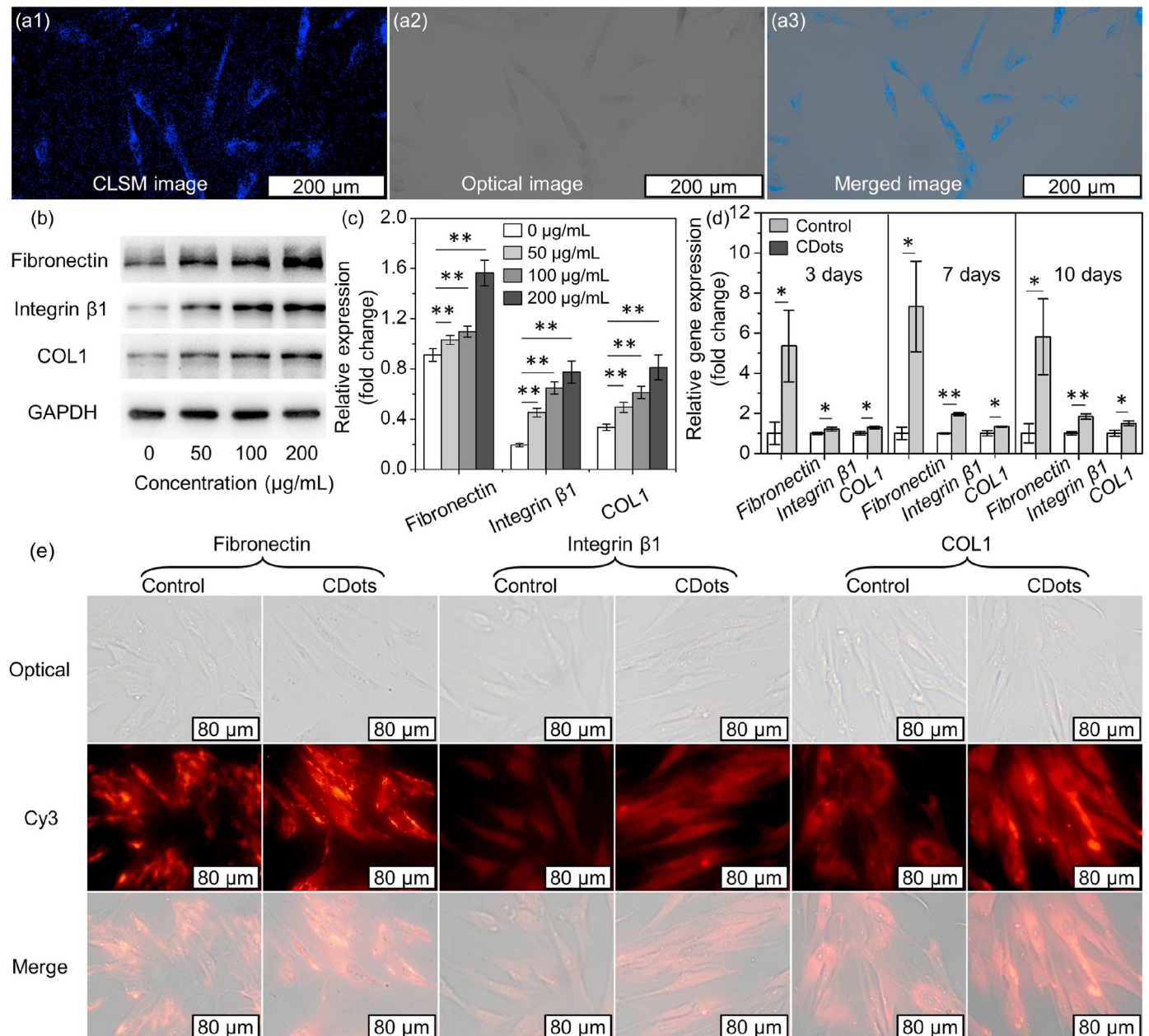

Fig. 2. Cell imaging of CDots-treated DPSCs and ECM secretion of DPSCs enhanced by CDots. (a) Cell imaging of CDots-treated DPSCs. (a1) CLSM image, (a2) optical image and (a3) merged image of optical and CLSM images. (b) Western blot analysis of ECM-related proteins: fibronectin, integrin β1 and COL1. (c) Corresponding quantitative data from Western blot. The relative expressions are fibronectin/GAPDH, integrin β1/GAPDH and COL1/GAPDH, respectively. (d) Detection of mRNA levels of *fibronectin*, *integrin β1* and *COL1* by RT-qPCR on day 3, 7 and 10. (e) Immunofluorescence staining for ECM-related proteins by fluorescence microscopy. Data are presented as mean ± SD from three independent experiments. * indicates $P < 0.05$, ** indicates $P < 0.01$.

DPSCs in a dose-dependent manner. Therefore, 200 μg/mL of CDots was determined to be used in the subsequent *in vitro* and *in vivo* studies. Reverse transcriptase quantitative polymerase chain reaction (RT-qPCR) assays were carried out to investigate the expression of ECM-related gene markers (Fig. 2d). All the gene expressions of *fibronectin, integrin β1*, and *COL1* significantly increased when CDots-treated DPSCs were cultured for 3, 7 and 10 days, respectively, which was consistent with the results

of Western blot. To more clearly visualize the variation of ECM, immunofluorescence staining was conducted through labeling the fibronectin, integrin β1, and COL1 by their respective primary antibodies, and then the primary antibodies were further combined with red fluorescent Cy3-labeled secondary antibody. In Fig. 2e and S8, after treating DPSCs with CDots, the red fluorescence intensities of these labeled proteins were obviously enhanced under the identical photo shooting conditions,
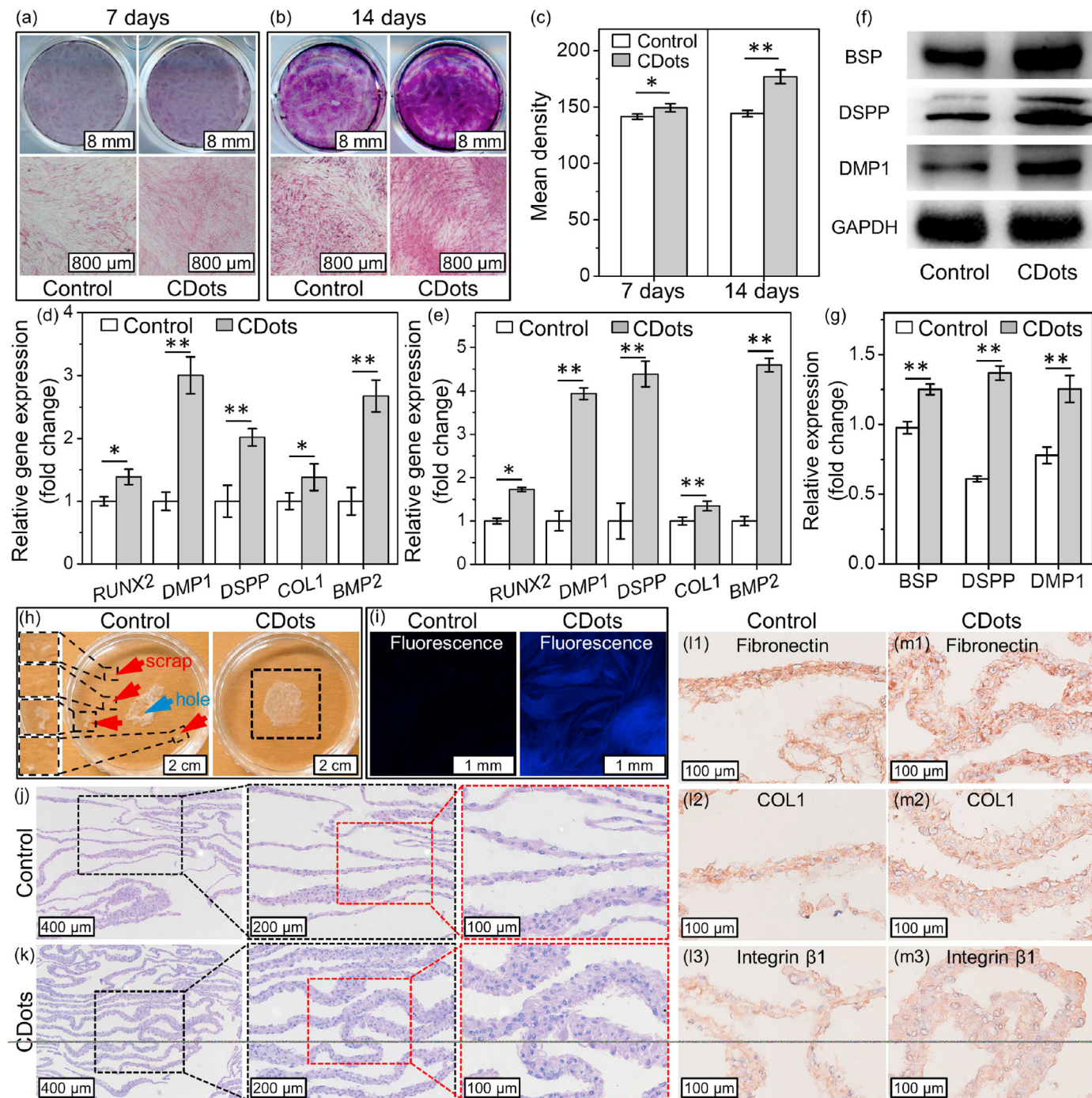

Fig. 3. Osteogenesis/odontogenesis of DPSCs and cell sheet formation induced by CDots. (a and b) ALP staining on day 7 and 14. (c) Corresponding quantitative data of ALP. (d and e) Validation of osteogenic/odontogenic genes expression by RT-qPCR on day 7 and 14. (f) Western blot analysis of osteogenic/odontogenic-related proteins: BSP, DSPP and DMP1. (g) Corresponding quantitative data from Western blot. The relative expressions are BSP/GAPDH, DSPP/GAPDH and DMP1/GAPDH, respectively. (h) Photographs of cell sheet, where the red and blue arrows represent the scraps and holes of the cell sheet in the control group, respectively. (i) Morphology of cell sheet observed by fluorescence microscope. (j and k) H&E staining of the cell sheet. (l and m) IHC staining of ECM-related proteins in the cell sheet. Data are presented as mean ± SD from three independent experiments. * indicates $P < 0.05$, ** indicates $P < 0.01$. (For interpretation of the references to colour in this figure legend, the reader is referred to the Web version of this article.)

including the exposure time and magnification times, therewith showing a similar CDots-induced expression increase of the ECM-related proteins. Besides, to evaluate the degradability of the CDots in the cell, we take advantage of the unique photoluminescent property of the CDots to trace their degradation (Fig. S9a). In experiments, DPSCs were cultured in a medium containing CDots for 24 h, after which the medium was removed, and these cells were washed twice with PBS and cultured in a fresh medium without CDots. Then, cell imaging of the DPSCs was carried out by confocal laser scanning microscopy at different time points (0, 2, 6, 12, 24, 36 and 48 h), and the distribution and degradation of the CDots were examined by tracing the blue fluorescence from CDots. The results demonstrate nearly no fluorescence outside the cells, suggesting that CDots were seldom excreted into ECM. Additionally, the intensity of blue fluorescence in the cells gradually went down with the increase of the culture time, and almost cannot be detected after 48 h, indicating that the CDots were degraded. The corresponding quantitative analysis of the fluorescence intensity also proves the above-mentioned conclusion (Fig. S9b). All of the above results demonstrate that our CDots can promote the ECM secretion of DPSCs.

The ECM constituents can usually bind and activate their receptors on the cell surface, and therewith amplify intracellular signal transduction for the osteogenic/odontogenic differentiation of DPSCs [42–44], suggesting that CDots with the capability of increasing ECM secretion are expected to promote the dentin-pulp complex regeneration. To evaluate the osteogenic/odontogenic differentiation capacity of DPSCs treated with CDots, two groups of DPSCs were first cultured in osteoinduction medium without or with CDots for 7 and 14 days, respectively, and then followed by alkaline phosphatase (ALP) staining, RT-qPCR and Western blot assays. As shown in Fig. 3a and b, higher ALP activity appeared in the CDots-treated cells than that in the control group, demonstrating an enhanced differentiation capacity of DPSCs induced by CDots, which was further confirmed by the corresponding quantitative analysis (Fig. 3c). Then, RT-qPCR assays were also performed to detect the expression of odontogenic gene markers (*i.e.*, dentin sialophosphoprotein (*DSPP*) and dentin matrix acidic phosphoprotein 1 (*DMP1*)) and osteogenic gene markers (namely, runt-related transcription factor 2 (*RUNX2*), *COL1* and bone morphogenetic protein 2 (*BMP2*)) (Fig. 3d and e). The results showed that CDots could significantly upregulate the expression of *RUNX2*, *DSPP*, *DMP1*, *COL1* and *BMP2* on day 7 and 14, indicating a stronger osteogenic/odontogenic differentiation capacity of CDots-treated DPSCs. The upregulated gene level again indicates that CDots can induce osteogenesis/odontogenesis of DPSCs through promoting ECM secretion. Furthermore, odontogenesis-related proteins (DMP1 and DSPP) and osteogenesis-related protein (bone sialoprotein (BSP)) were evaluated by Western blot assay (Fig. 3f and g). Compared to the control group, DMP1 and DSPP proteins displayed higher expressions in the CDots group, demonstrating that the presence of CDots facilitated the odontogenic differentiation of DPSCs [45,46]. BSP is a mineralized tissue specific protein and its increased expression in the CDots group proves the potential of CDots-treated DPSCs for the osteogenesis, resulting in the formation of mineralized tissues (*i.e.*, dentin) [47]. The above results demonstrate that CDots-treated DPSCs possess a stronger osteogenic/odontogenic differentiation capacity, thus laying the foundation for their further *in vivo* applications in the dentin-pulp complex regeneration [48].

Apart from being a biochemical signal provider, ECM, as a structural scaffold, is responsible for the cell-ECM adhesion, so the enhancement of ECM secretion is beneficial to the formation of cell sheet, which is an important way for tissue regeneration [49]. Besides, we further examined the expression of E-cadherin, one classification of cell adhesion molecules. E-cadherin is essential for the cell-cell connection, which is also important for the formation of cell sheet. As shown in Fig. S10, the expression of E-cadherin appeared an obvious upregulation in DPSCs treated with CDots. Combining the quantitative analysis of Western blot assay and immunofluorescence staining (Fig. 2c and Fig. S8), the obvious upregulation of these ECM-related proteins suggests that CDots can

promote cell-cell connections as well as cell-ECM adhesions. Then, after treating DPSCs with CDots for 10 days, the formation of an intact dental pulp stem cell sheet was observed and the cell sheet was easily detached from the bottom of the culture dish (Fig. 3h). In contrast, the DPSCs without treatment by CDots only formed a broken cell sheet with an obvious hole, with lots of scraps accumulated around the cell sheet. To better clarify this difference, the number of the scraps of the cell sheets in the control and CDots groups are quantified, respectively. Five cell sheets were processed in the control and CDots group separately, and then we checked the number of the scraps. As shown in Fig. S11, the number of the scraps in the control group is 8.4, while there is nearly no scraps in the CDots group (*i.e.*, an intact cell sheet is usually obtained in the CDots group). This comparison further suggests that the cell sheet in the CDots group possesses tighter cell-cell connections. Besides, the blue fluorescence of cell sheet could be observed with an ultraviolet excitation (Fig. 3i), indicating that CDots play a key role in the process of cell sheet formation. Next, hematoxylin and eosin (H&E) staining technology was performed to examine the internal morphology and structure of the cell sheet. As shown in Fig. 3j, k and Fig. S12, the thickness of the cell sheet in the CDots group was approximately 2.5 times higher than that of the control group. Considering CDots were found to have no effects on the proliferation and apoptosis of DPSCs (Fig. 1g and i), the thicker cell sheet in the CDots group should be attributed to more ECM promoted by CDots. To verify this assumption, immunohistochemical (IHC) staining and its corresponding quantitative analysis were conducted to investigate the amount of ECM components, and the results manifested that the CDots-induced cell sheet exhibited more ECM deposition than that of the control group (Fig. 3l, m and Fig. S13), and these more ECM are also responsible for the tighter cell-cell connections.

3.4. CDots-induced activation of autophagy via regulating PI3K/Akt/mTOR pathway contributes to the ECM secretion of DPSCs

Having established that CDots can promote the ECM secretion, we next explored the mechanisms underlying this process by RNA sequencing (RNA-seq)-based transcriptome analysis. Compared with the control groups, 35 kinds of differentially expressed genes were identified in DPSCs treated with CDots based on the fold changes and *P*-values (Fig. 4a). Then, Kyoto Encyclopedia of Genes and Genomes (KEGG) pathway enrichment analysis was performed on these differentially expressed genes to identify the major biological functions or pathways, during which 10 kinds of differentially expressed genes (*i.e.*, *PTPRB*, *SLX1A*, *ADRA1D*, *ICOSLG*, *NMNAT2*, *CBSL*, *F2RL3*, *FOXA2*, *CYP1A1*, and *CYP1B1*) were successfully enriched in 28 signal transduction pathways (Fig. 4b). Among these 10 differentially expressed genes, *FOXA2* was a transcription factor and exhibited higher expression in CDots group, which was further confirmed by RT-qPCR analysis (Fig. S14). Besides, *FOXA2* was enriched in the longevity regulating pathway, where the upregulation of *FOXA2* could activate autophagy (Fig. 4c). On the other hand, several studies have proved that a reasonable activation of the autophagy can efficiently increase the ECM secretion [50–53]. Thus, the increase of the ECM secretion in the CDots-treated DPSCs is expected to be because of the CDots-induced activation of autophagy, which is indicated by the *FOXA2* upregulation.

To validate the hypothesis that CDots induced the activation of autophagy and therewith facilitated the ECM secretion, the Western blot assay was performed. As shown in Fig. 4d and S15a, compared to the control group, the Beclin1 and LC3II, as well-known autophagy markers, appeared higher expression after incubating DPSCs with CDots for 6, 12 and 24 h, respectively. Correspondingly, the expression of P62, which is a hallmark of autophagy substrate, presented a decreased level after treating DPSCs with CDots, signifying a depletion of autophagy substrate. Combining the results of Beclin1/LC3II and P62, it is demonstrated that the as-prepared CDots can activate the autophagy. Besides, ascorbic acid and PEI were also applied to evaluate their effects on the activation of autophagy. By performing the cytotoxicity assay (Fig. S16), the
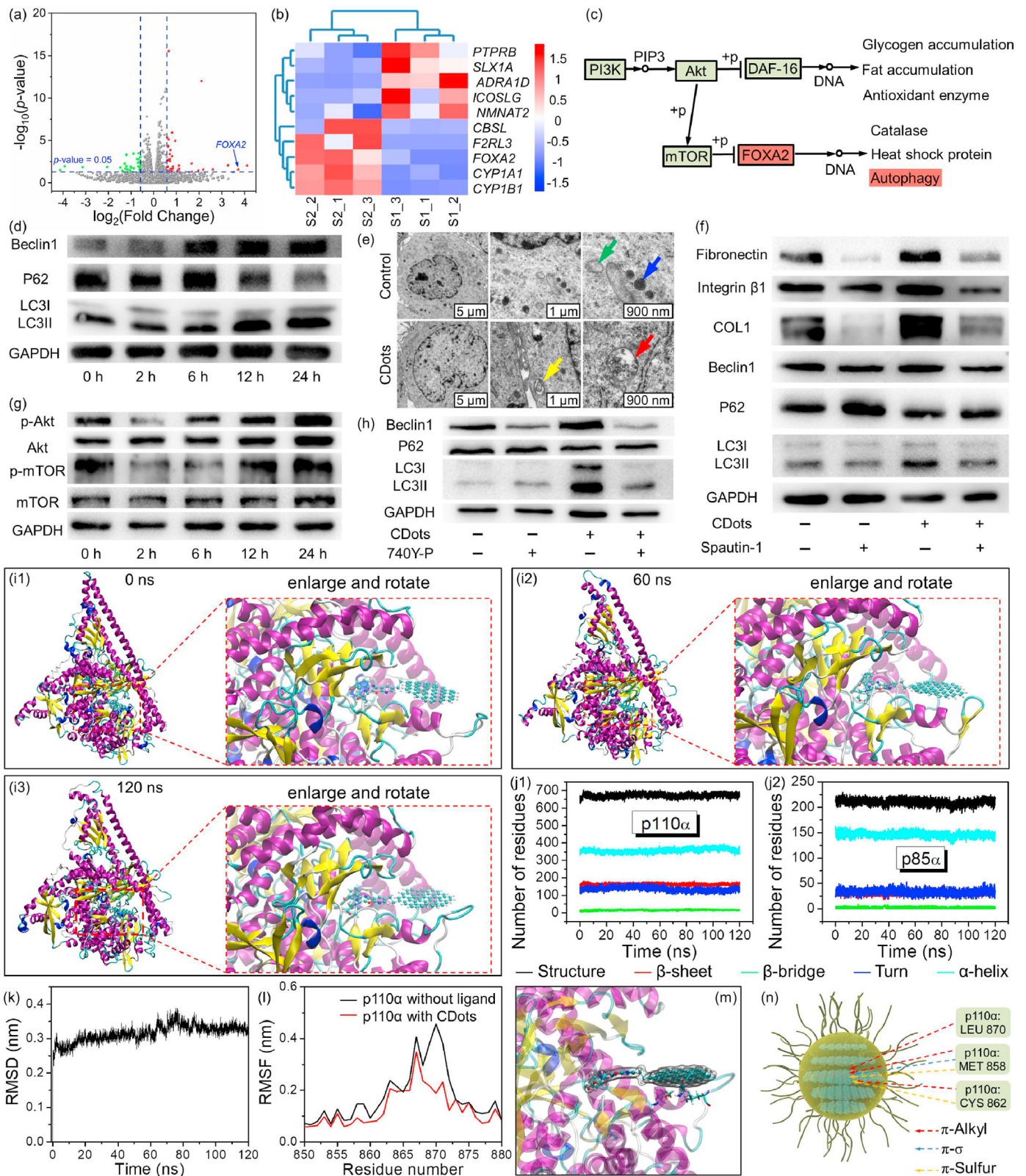
(caption on next page)

Fig. 4. CDots-promoted ECM secretion by activating autophagy *via* regulating PI3K/Akt/mTOR pathway. (a) Volcano diagram and (b) heat map of differentially expressed genes. (c) Signaling pathway where *FOXA2* is enriched. (d) Western blot results of autophagy-related proteins (Beclin1 and LC3B) and autophagy substrate protein (P62) in DPSCs treated with CDots (200 μg/mL) from 0 to 24 h. (e) TEM images. Blue arrow indicates lysome, green arrow indicates mitochonsria, yellow arrow indicates autophagosome, and red arrow indicates autolysosomes. The two images in the left panel are taken under low magnification, and the images in the middle and right panels, which are taken under high magnification, are the enlargement of several specific areas of the corresponding images in the left panel. (f) Western blot results of Beclin1, P62, LC3B and ECM-related proteins (fibronectin, integrin β1, and COL1) in DPSCs treated without or with CDots (200 μg/mL) and spautin-1, respectively. (g) Western blot results of p-Akt, Akt, p-mTOR, and mTOR. DPSCs were treated without or with CDots (200 μg/mL) from 0 to 24 h. (h) Western blot results of Beclin1, P62, LC3B in DPSCs treated without or with CDots (200 μg/mL) and 740Y–P, respectively. (i) The structures of CDots binding to p110α/p85α complex, which are extracted from the molecular dynamics simulation trajectory at 0, 60, and 120 ns, respectively. Secondary structural elements are depicted as ribbons. Color is based on secondary structures (α-helix, purple; 3–10 helix, blue; β-sheets, yellow; turn, cyan; coil, white). (j) The numbers of residues in diverse secondary structures of (j1) p110α and (j2) p85α. (k) RMSD of the Cα atoms of p110α/p85α in p110α/p85α/CDots complex against time. (l) RMSF values of p110α in the p110α/p85α complex and p110α/p85α/CDots complex, respectively. (m) 3D diagram of interaction between CDots and p110α. Amino acid residues involved in the binding of CDots are drawn as sticks, and CDots are shown as ball-and-stick model. Carbon, hydrogen, oxygen and nitrogen atoms are colored in green, gray, red and blue, respectively. (n) 2D diagram of interaction between CDots and p110α. Interactions involved in the binding of CDots to amino acid residues are shown as dashed lines in different corresponding colors. Data are presented as mean ± SD from three independent experiments. * indicates $P < 0.05$, ** indicates $P < 0.01$. "−" and "+" symbols represent "without" and "with," respectively. (For interpretation of the references to colour in this figure legend, the reader is referred to the Web version of this article.)

concentrations of ascorbic acid and PEI for treating DPSCs were determined to be 200 and 20 μg/mL, respectively, and the results of Western blot assay showed that the expressions of LC3II and P62 were unchanged, indicating that both ascorbic acid and PEI failed to induce autophagy of DPSCs (Fig. S17). To further determine if autophagy occurs in the CDots-treated DPSCs, autophagosome or autolysosome was detected by morphological observation using TEM. As shown in Fig. 4e, the number of mature autophagosomes or autolysosomes was increased in CDots-treated DPSCs, suggesting the stimulation of autophagy by CDots in DPSCs. These results demonstrate that CDots can promote autophagy in DPSCs. To further clarify the correlation between CDots-activated autophagy and ECM secretion, spautin-1, the inhibitor of autophagy, was adopted to evaluate whether the increase of ECM secretion could still be caused by CDots. As seen from the results of Western blot, after the addition of spautin-1, the DPSCs treated by CDots presented an obvious decrease in ECM secretion owing to a decline in the level of the autophagy in comparison with the sole CDots group (Fig. 4f and S15b). Based on these results, it is safe to conclude that the enhancement of the ECM secretion promoted by CDots can be attributed to the activation of the autophagy.

Furthermore, the KEGG pathway enrichment analysis indicates that the CDots-induced activation of the autophagy is closely related to the PI3K/Akt/mTOR pathway (Fig. 4c), which inspires us to clarify the correlation between CDots and the PI3K/Akt/mTOR pathway. In the normal cellular activity, various growth factors can activate their receptor tyrosine kinases or G protein-coupled receptors, resulting in the combination of these receptors with the SH2 domain of the adaptor proteins. Then, the adaptor proteins will recruit the intracellular PI3K proteins to the plasma membrane, after which the catalytic subunit (p110α) of PI3K protein can trigger the phosphorylation of the downstream Akt and mTOR. According to previous reports [54] and Fig. 4c, if the catalytic subunit (p110α) of PI3K protein can be inhibited to some extent, the phosphorylation levels of the Akt and mTOR would be downregulated, leading to a reasonable activation of the autophagy and the promotion of the ECM secretion thereof (Fig. 4f). To illustrate the correlation between CDots-induced autophagy and the PI3K/Akt/mTOR pathway, we first evaluated the effect of CDots on the phosphorylation levels of the Akt and mTOR, and the corresponding results proved that the induction of CDots could obviously decrease the phosphorylation levels of the Akt and mTOR (Fig. 4g and S18a), indicating the suppression of the PI3K/Akt/mTOR pathway. To further confirm the role of this pathway in CDots-activated autophagy, SC79, a highly potent Akt activator which could prevent the activation of the autophagy, was applied. As evidenced in Fig. S18c and d, sole SC79 would not change the autophagy level of DPSCs, and the autophagy level in DPSCs treated by CDots could be raised. However, after adding SC79, the autophagy level in DPSCs treated by CDots presented an obvious decreased level, indicating that CDots-induced autophagy was mainly conducted through the

inhibition of Akt/mTOR pathway. At this stage, there are two possible causes for blocking the Akt/mTOR pathway: (1) the presence of a direct interaction between CDots and Akt protein; and (2) preventing the signal transduction of the upstream PI3K protein by CDots. In order to address this issue, 740Y–P, an activator of PI3K to suppress the activation of autophagy, was adopted to evaluate whether CDots-induced autophagy could still be triggered by the PI3K pathway. If the addition of 740Y–P has no effects on the CDots-activated autophagy, the autophagy induced by CDots should be due to the interaction of CDots with Akt protein. Otherwise, the autophagy caused by CDots should be owing to the prohibition of the signal transduction of the upstream PI3K protein by CDots. As shown in Fig. 4h and S18b, DPSCs treated by CDots appeared a high autophagy level, while the autophagy level declined after adding 740Y–P. All these results suggest that CDots could interact with PI3K, which can inhibit the PI3K/Akt/mTOR pathway, activate the autophagy, and finally promote the ECM secretion.

As mentioned above, the activation of the catalytic subunit (p110α) of intracellular PI3K protein is usually the start of the PI3K pathway, so the inhibitory activity of CDots on this pathway indicates that CDots could interact with p110α protein, which can be further understood as follows. According to the cell imaging in Fig. 2a, our CDots could be internalized into the cells, and p110α is a kind of intracellular protein, thus providing a foundation for their combination. Furthermore, p110α has negative charges, whereas the zeta potential of CDots was positive (Fig. S2), so there is electrostatic attraction between p110α and CDots. More importantly, as reported previously, the amino acid residues around the binding site of p110α generally interact with those five/six-membered aromatic/heterocyclic compounds, which are composed of carbon, nitrogen and oxygen atoms, to form a stable complex, thereby blocking the pathway [55–57]. Based on HRTEM, FTIR and XPS analysis, our CDots, synthesized by ascorbic acid and PEI, possessed a graphene-like carbonized core (Fig. 1c–f), and the long-chain alkyl amine structures of PEI and the furanose ring structure of ascorbic acid allow the formation of aromatic and nitrogen/oxygen heterocyclic groups on the surface of the CDots [58–60]. By combining the results of inhibiting the PI3K pathway by CDots and the structural features of the CDots, it is reasonable to conclude that our CDots could interact with p110α protein to form a stable complex. Despite these promising results, the nanosized graphene-like carbonized core may raise concern about the steric hindrance to the complex formation, so the role of the graphene-like carbonized core in this process should be clarified. PI3K proteins are heterodimeric molecules composed of a catalytic subunit (p110α) and a regulatory subunit (p85α), namely, p110α protein is always accompanied with the regulatory subunit (p85α), and then it is essential to illustrate whether the p85α protein has an influence on the binding of CDots with p110α. To address these issues, molecular dynamics simulation was adopted to assess the structural stability. Before the simulation, an initial model was established using the structures from RCSB Protein Data Bank

(PDB) website (PDB ID: 4ovu), and a graphene-like fragment was attached to the ligand molecule as a simplified model of CDots (Fig. S19a and b). It is worth mentioning that because there are several missing amino acid residues in the original three-dimensional structures of p110α and p85α (PDB ID: 4ovu), the structures of p110α and p85α were constructed using the homology modeling method (Fig. S20c and d). Ramachandran plot was applied to verify the predicted torsion angles in these two constructed proteins. As shown in Fig. S20a and b, 99% of residues in these two proteins were located in the Allowed Region for the Ramachandran plot, demonstrating a good quality model [61,62]. Then, a 120 ns of molecular dynamics simulation was performed. The animated movie of the p110α/p85α/CDots complex, based on 600 frames extracted from the trajectory, was provided in Movie S1. As seen from the movie and the snapshot images of the simulation trajectory at 0, 60 and 120 ns (Fig. 4i), CDots didn't separate from the p110α/p85α complex in the whole simulation time. The root mean square deviation (RMSD) of the backbone atoms in the complex after a least-squares fit to the initial structure was calculated over the whole trajectory to further confirm the structural stability. The RMSD value was found to change rapidly to 2.8 Å at 2.5 ns and then started stabilizing at approximately 3.5 Å from 75 ns with a minor fluctuation (Fig. 4k). Meanwhile, the numbers of residues in diverse secondary structures of p110α and p85α, including α-helix, turn, β-sheet and β-bridge, were nearly unchanged during the simulation (Fig. 4j). The result indicates the existence of the nanosized carbonized core and p85α has no adverse effects on the combination. On the contrary, by analyzing the interactions, it was found that the graphene-like fragment was favorable to anchor CDots into p110α. Subsequently, the residue-wise root mean square fluctuation (RMSF), which reflects the deviation of the position of the amino acid residues in p110α, was further detected. Before evaluating the RMSF of the complex, a 120 ns of molecular dynamics simulation of the sole p110α/p85α complex without ligand was carried out (Fig. S21 and Movie S2), in which the RMSF values of p110α in sole p110α/p85α complex served as a reference for the comparison. The RMSD curve and number of residues in various secondary structures of the sole p110α/p85α complex were displayed in Fig. S21, suggesting that the stable conformation was achieved after 20 ns simulation. Then, to calculate RMSF, the simulation trajectories of both the p110α/p85α/CDots complex and the p110α/p85α complex without ligand were obtained from the last stable 20 ns of the molecular dynamics simulation. As shown in Fig. 4l, the RMSF values of p110α in the p110α/p85α/CDots complex were obviously lower compared with p110α in the sole p110α/p85α complex, indicating that the amino acid residues of p110α in the p110α/p85α/CDots complex were restrained, namely, there were several interactions between CDots and p110α. To directly observe the detailed binding mode between the graphene-like fragment and p110α protein, we visualized the final structure of the simulation trajectory using the Visual Molecular Dynamics (VMD) program, and displayed the three-dimension (3D) and two-dimension (2D) interaction diagrams (Fig. 4m, n and Movie S3), respectively. As shown in the 2D diagram, thanks to the large π-conjugated structure in the graphene-like fragment, there were various van der Waals interactions between CDots and p110α, including π-sulfur interaction with MET858 and CYS862, π-σ interaction with MET858, and π-alkyl interactions with MET858, CYS862 and LEU870. By combining these results, the existence of the strong interaction between CDots and p110α is verified and thus induces the autophagy to some extent, leading to an obvious increase in the secretion of ECM.

Supplementary video related to this article can be found at https://doi.org/10.1016/j.mtbio.2022.100344

3.5. In vivo regeneration of dentin-pulp complex

Inspired by the CDots-promoted ECM secretion and osteogenesis/odontogenesis of DPSCs, we applied CDots to promote *in vivo* the differentiation of DPSCs into odontoblasts and the dentin-pulp complex regeneration [5,48,63]. To evaluate the effects of CDots on dentin-pulp

complex regeneration, an ectopic transplantation model was established. In detail, human premolars were first treated to obtain human treated dentin matrix fragments (hTDMFs) as described in experimental section, and then the root canal space of hTDMFs was filled with untreated DPSCs-based cell sheet (named as the untreated DPSCs group) or CDots-induced DPSCs-based cell sheet with abundant ECM (named as the CDots-treated DPSCs group), while hTDMFs without any treatments were defined as the control group. Finally, the whole composites as an implant were transplanted subcutaneously into the immunocompromised mice and harvested after 15 weeks (Fig. 5a). Histological examinations of these implants revealed that only subcutaneous adipose tissue was observed in the canal space of the control group (Fig. 5b and e), whereas newly-formed dentin-pulp like tissues could be found in the untreated DPSCs and the CDots-treated DPSCs groups. Nevertheless, compared to the untreated DPSCs group (Fig. 5c and f), there were more pre-dentin and more mineralized tissue deposition on the existing dentinal wall of the hTDMF in the CDots-treated DPSCs group (Fig. 5d and g), as reflected by the quantitative analysis showing a near twofold increase (Fig. S22). At a higher magnification, the H&E staining images of the untreated DPSCs group, which were taken at different positions, showed few odontoblast-like cells in No.3 area, even none in No.1 and 2 area, while lots of odontoblast-like cells lining the regenerated dentin-like tissue could be observed in the CDots-treated DPSCs group. As discussed in Fig. 3, our CDots could enhance the osteogenic/odontogenic differentiation capacity of DPSCs through promoting ECM secretion, and thus facilitate the differentiation of more DPSCs into odontoblast-like cells under induction of hTDMFs in the CDots-treated DPSCs group. To verify this in *in vivo* study, IHC staining was conducted and the results indicate that the expressions of DSPP and DMP1 proteins display obvious upregulations in the CDots-treated DPSCs group compared to that in the untreated DPSCs group (Fig. 5h, i, k and l), proving the presence of plenty of odontoblast-like cells. As a result, these odontoblast-like cells in the CDots-treated DPSCs group could secret abundant dentin matrix, which was further proved by Masson's trichrome staining (Fig. 5g). On the other hand, the dentin is usually originated from the dentin matrix mineralization [64], so the existence of the abundant dentin matrix in the CDots-treated DPSCs group is responsible for the formation of more dentin. These results indeed confirm that DPSCs with stronger odontogenic/osteogenic differentiation potential are more liable to differentiate into odontoblast cells and promote the mineralization and formation of more dentin from extracellular matrix. The H&E staining images of the CDots-treated DPSCs group also presented the formation of several blood vessels (Fig. 5d), where the abundant ECM, known as mediators of vessel formation, played a pivotal role in the angiogenic process [65], but these blood vessels couldn't be discovered in another two groups. The corresponding results of IHC staining showed that the platelet endothelial cell adhesion molecule-1 (CD31), as a vascularization-related marker, was positive only in the CDots-treated DPSCs group (Fig. 5j and m), also proving the formation of blood vessels, namely the regeneration of the functional dental pulp [5,48].

Taken together, these data suggest that DPSCs treated by CDots hold great potential in promoting efficient regeneration of dentin-pulp complex *in vivo*. Last, to investigate whether the CDots cause side effects *in vivo*, H&E staining of important organs was performed (Fig. S23). The result demonstrates that there is no histological abnormality in heart, liver, spleen and kidney of the CDots-treated DPSCs group, indicating that CDots are safe for *in vivo* applications.

4. Conclusion

In summary, we synthesized CDots *via* a one-pot hydrothermal treatment of ascorbic acid and PEI. The obtained CDots possessed blue photoluminescence, abundant functional groups, and excellent biocompatibility. Through transcriptome analysis, Western blot assay and molecular dynamics simulation, it was demonstrated that our CDots could enhance the ECM secretion of DPSCs *via* the PI3K/Akt/mTOR pathway-
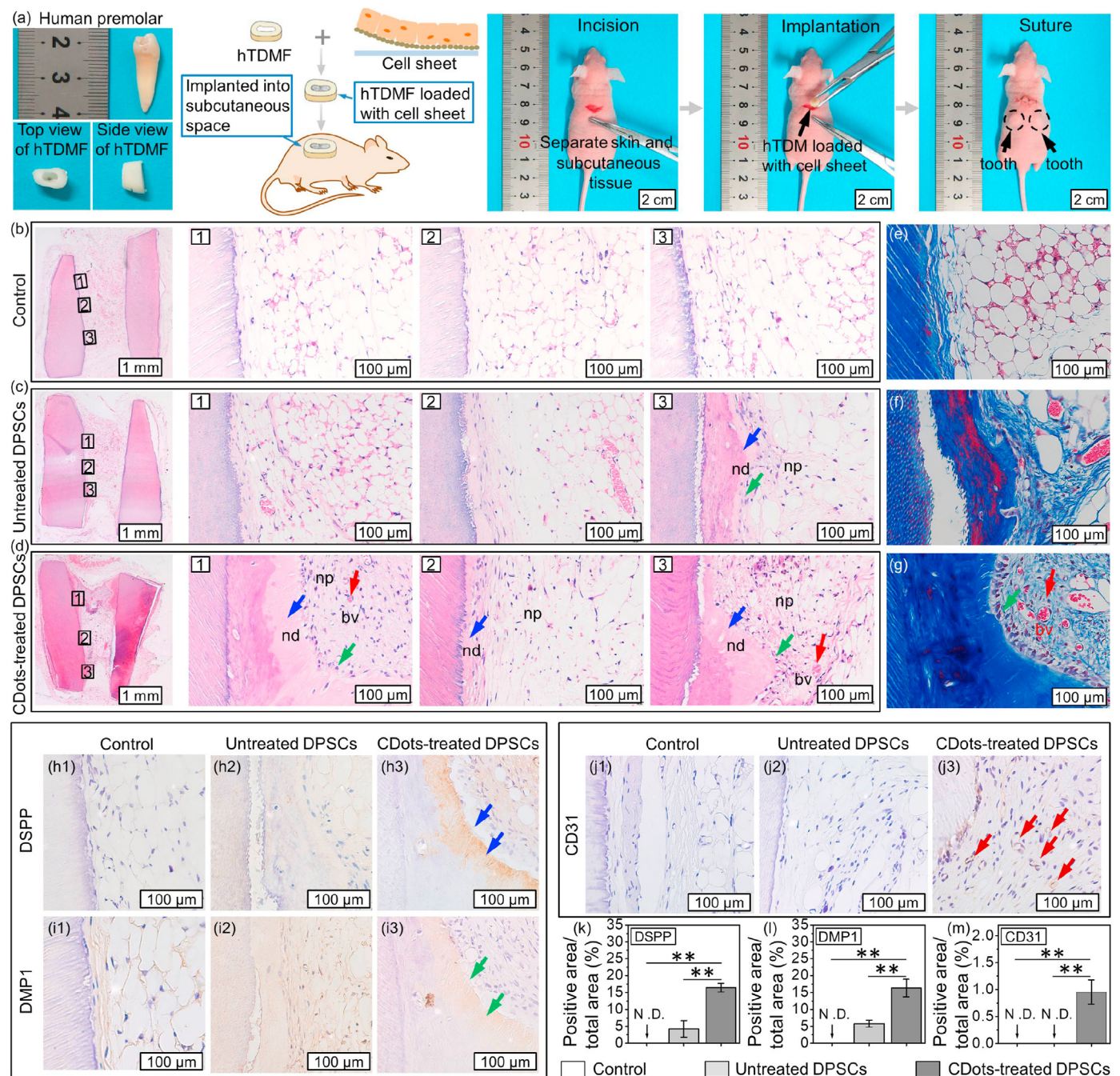
Fig. 5. CDots-induced cell sheet enabled regeneration of dentin-pulp complex tissue *in vivo*. (a) Schematic diagram of hTDMF transplantation in nude mice. Cell sheet was inserted into hTDMF before subcutaneously transplanted into nude mice. (b–d) H&E staining for histological analysis of tissues regenerated in hTDMF after subcutaneous transplantation: (b) control group, (c) untreated DPSCs group and (d) CDots-treated DPSCs group. Blue arrows show the newly formed dentin. Green arrows show odontoblast-like cells that aligned the newly formed dentin surface. Red arrows present the newly formed blood vessel. nd, newly formed dentin; np, new formed pulp; bv, blood vessel. (e–g) Masson's Trichrome staining: (e) control group, (f) untreated DPSCs group and (g) CDots-treated DPSCs group. Green arrows show odontoblast-like cells that aligned the newly formed dentin surface. Red arrows present the newly formed blood vessel. (h–m) IHC staining of DSPP, DMP1 and CD31 and the quantitative analysis. Blue arrows show DSPP. Green arrows show DMP1. Red arrows show CD31-positive cells. Data are presented as mean ± SD from three independent experiments. ** indicates $P < 0.01$. N.D., not detected. (For interpretation of the references to colour in this figure legend, the reader is referred to the Web version of this article.)

mediated reasonable activation of autophagy. The abundant ECM brought by CDots can enhance the cell adhesion on ECM, facilitate the formation of an intact dental pulp stem cell sheet with a strong osteogenic/odontogenic differentiation capacity, and therewith promote *in vivo* the efficient regeneration of dentin-pulp complex as well as blood vessels, showing that the CDots demonstrated here hold unique advantages as a novel nanoparticle-based medicine for addressing the clinical

diseases, and further contribute new insights into discovery in pharmaceutical research.

Credit author statement

Lili Liu: Conceptualization, Methodology, Investigation, Writing – original draft, Writing – review & editing. Xianjing Li: Methodology, Data

curation, Software. Wenhuan Bu: Formal analysis, Software. Nianqiang Jin: Data curation, Investigation. Yuan Meng: Investigation, Visualization. Yi Wang: Formal analysis, Investigation. Duan Wang: Data curation, Software. Xiaowei Xu: Resources, Methodology, Project administration, Validation, Writing – review & editing. Ding Zhou: Funding acquisition, Project administration, Validation, Writing – review & editing. Hongchen Sun: Resources, Funding acquisition, Project administration, Validation, Conceptualization, Supervision, Writing – review & editing.

Data availability

The data that support the figures within this paper and other findings of this study are available from the corresponding author upon reasonable request.

Declaration of competing interest

The authors declare that they have no known competing financial interests or personal relationships that could have appeared to influence the work reported in this paper.

Acknowledgements

Appendix B. Supplementary data

Supplementary data to this article can be found online at https://doi.org/10.1016/j.mtbio.2022.100344.

References

[1] M.A. Peres, L.M.D. Macpherson, R.J. Weyant, B. Daly, R. Venturelli, M.R. Mathur, S. Listl, R.K. Celeste, C.C. Guarnizo-Herreño, C. Kearns, H. Benzian, P. Allison, R.G. Watt, Oral diseases: a global public health challenge, Lancet 394 (2019) 249–260.

[2] M.A. Taubman, D.A. Nash, The scientific and public-health imperative for a vaccine against dental caries, Nat. Rev. Immunol. 6 (2006) 555–563.

[3] European Society of Endodontology, Quality guidelines for endodontic treatment: consensus report of the european society of endodontology, Int. Endod. J. 39 (2006) 921–930.

[4] Z.W. Li, T.M. Du, C.S. Ruan, X.F. Niu, Bioinspired mineralized collagen scaffolds for bone tissue engineering, Bioact. Mater. 6 (2021) 1491–1511.

[5] H. Chen, H.C. Fu, X. Wu, Y.F. Duan, S.C. Zhang, H. Hu, Y.S. Liao, T. Wang, Y. Yang, G.Q. Chen, Z.H. Li, W.D. Tian, Regeneration of pulpo-dentinal-like complex by a group of unique multipotent CD24a⁺ stem cells, Sci. Adv. 6 (2020), eaay1514.

[6] N. Matsuda, T. Shimizu, M. Yamato, T. Okano, Tissue engineering based on cell sheet technology, Adv. Mater. 19 (2007) 3089–3099.

[7] X.W. Li, C. Ma, X.H. Xie, H.C. Sun, X.H. Liu, Pulp regeneration in a full-length human tooth root using a hierarchical nanofibrous microsphere system, Acta Biomater. 35 (2016) 57–67.

[8] Y. Inuyama, C. Kitamura, T. Nishihara, T. Morotomi, M. Nagayoshi, Y. Tabata, K. Matsuo, K.K. Chen, M. Terashita, Effects of hyaluronic acid sponge as a scaffold on odontoblastic cell line and amputated dental pulp, J. Biomed. Mater. Res., Part B 92 (2010) 120–128.

[9] H. Ishimatsu, C. Kitamura, T. Morotomi, Y. Tabata, T. Nishihara, K.K. Chen, M. Terashita, Formation of dentinal bridge on surface of regenerated dental pulp in dentin defects by controlled release of fibroblast growth factor-2 from gelatin hydrogels, J. Endod. 35 (2009) 858–865.

[10] D.G. Moussa, C. Aparicio, Present and future of tissue engineering scaffolds for dentin-pulp complex regeneration, J. Tissue Eng. Regener. Med. 13 (2019) 58–75.

[11] R.O. Hynes, The extracellular matrix: not just pretty fibrils, Science 326 (2009) 1216–1219.

[12] H.F. Meng, L. Hu, Y. Zhou, Z.Q. Ge, H. Wang, C.-T. Wu, J.D. Jin, A sandwich structure of human dental pulp stem cell sheet, treated dentin matrix and matrigel for tooth root regeneration, Stem Cell. Dev. 29 (2020) 521–532.

[13] L. Hu, B. Zhao, Z.H. Gao, J.J. Xu, Z.P. Fan, C.M. Zhang, J.S. Wang, S.L. Wang, Regeneration characteristics of different dental derived stem cell sheets, J. Oral Rehabil. 47 (Suppl. 1) (2020) 66–72.

[14] S.J. Na, H. Zhang, F. Huang, W.Q. Wang, Y. Ding, D.C. Li, Y. Jin, Regeneration of dental pulp/dentine complex with a three-dimensional and scaffold-free stem-cell sheet-derived pellet, J. Tissue Eng. Regener. Med. 10 (2016) 261–270.

[15] C. Schmid, H.P. Guler, D. Rowe, E.R. Froesch, Insulin-like growth factor I regulates type I procollagen messenger ribonucleic acid steady state levels in bone of rats, Endocrinology 125 (1989) 1575–1580.

[16] N. Maeda, F. Kanda, S. Okuda, K. Ishihara, K. Chihara, Transforming growth factor-β enhances connective tissue growth factor expression in L6 rat skeletal myotubes, Neuromuscul. Disord. 15 (2005) 790–793.

[17] R.H. Jing, T.T. Qi, C. Wen, J.Q. Yue, G.Y. Wang, C. Pei, B. Ma, Interleukin-2 induces extracellular matrix synthesis and TGF-β2 expression in retinal pigment epithelial cells, Dev. Growth Differ. 61 (2019) 410–418.

[18] J. Coyne, N. Zhao, A. Olubode, M. Menon, Y. Wang, Development of hydrogel-like biomaterials *via* nanoparticle assembly and solid-hydrogel transformation, J. Contr. Release 318 (2020) 185–196.

[19] N. Stone, A. Meister, Function of ascorbic acid in the conversion of proline to collagen hydroxyproline, Nature 194 (1962) 555–557.

[20] H.J. Liu, X.T. Lv, J.C. Qian, H. Li, Y. Qian, X.Y. Wang, X.F. Meng, W.C. Lin, H. Wang, Graphitic carbon nitride quantum dots embedded in carbon nanosheets for near-infrared imaging-guided combined photo-chemotherapy, ACS Nano 14 (2020) 13304–13315.

[21] B.L. Li, S.J. Zhao, L. Huang, Q. Wang, J.F. Xiao, M.H. Lan, Recent advances and prospects of carbon dots in phototherapy, Chem. Eng. J. 408 (2021), 127245.

[22] S.Y. Tao, S.Y. Lu, Y.J. Geng, S.J. Zhu, S.A.T. Redfern, Y.B. Song, T.L. Feng, W.Q. Xu, B. Yang, Design of metal-free polymer carbon dots: a new class of room-temperature phosphorescent materials, Angew. Chem., Int. Ed. 57 (2018) 2393–2398.

[23] J.L. Chen, J. Yan, Q.M. Feng, X.M. Miao, B.T. Dou, P. Wang, Label-free and enzyme-free fluorescence detection of microRNA based on sulfydryl-functionalized carbon dots *via* target-initiated hemin/G-quadruplex-catalyzed oxidation, Biosens. Bioelectron. 176 (2021), 112955.

[24] N. Soni, S. Singh, S. Sharma, G. Batra, K. Kaushik, C. Rao, N.C. Verma, B. Mondal, A. Yadav, C.K. Nandi, Absorption and emission of light in red emissive carbon nanodots, Chem. Sci. 12 (2021) 3615–3626.

[25] Y.L. Xu, Y. Yang, S. Lin, L.H. Xiao, Red-emitting carbon nanodot-based wide-range responsive nanothermometer for intracellular temperature sensing, Anal. Chem. 92 (2020) 15632–15638.

[26] Y.B. Yan, J. Gong, J. Chen, Z.P. Zeng, W. Huang, K.Y. Pu, J.Y. Liu, P. Chen, Recent advances on graphene quantum dots: from chemistry and physics to applications, Adv. Mater. 31 (2019), 1808283.

[27] G. Rath, T. Hussain, G. Chauhan, T. Garg, A.K. Goyal, Collagen nanofiber containing silver nanoparticles for improved wound-healing applications, J. Drug Target. 24 (2016) 520–529.

[28] K.S. Brammer, S. Oh, C.J. Frandsen, S. Varghese, S. Jin, Nanotube surface triggers increased chondrocyte extracellular matrix production, Mater. Sci. Eng., C 30 (2010) 518–525.

[29] S. Luanpitpong, L.Y. Wang, Y. Rojanasakul, The effects of carbon nanotubes on lung and dermal cellular behaviors, Nanomedicine 9 (2014) 895–912.

[30] A. Mishra, Y. Rojanasakul, B.T. Chen, V. Castranova, R.R. Mercer, L.Y. Wang, Assessment of pulmonary fibrogenic potential of multiwalled carbon nanotubes in human lung cells, J. Nanomater. 2012 (2012) 1–11.

[31] X. Wang, T. Xia, S.A. Ntim, Z.X. Ji, S.J. Lin, H. Meng, C.H. Chung, S. George, H.Y. Zhang, M.Y. Wang, N. Li, Y. Yang, V. Castranova, S. Mitra, J.C. Bonner, A.E. Nel, Dispersal state of multiwalled carbon nanotubes elicits profibrogenic cellular responses that correlate with fibrogenesis biomarkers and fibrosis in the murine lung, ACS Nano 5 (2011) 9772–9787.

[32] Y. Zhang, S.N. Wang, F. Lu, M.L. Zhang, H. Kong, J.J. Cheng, J. Luo, Y. Zhao, H.H. Qu, The neuroprotective effect of pretreatment with carbon dots from *Crinis Carbonisatus* (carbonized human hair) against cerebral ischemia reperfusion injury, J. Nanobiotechnol. 19 (2021) 257.

[33] S.C. Liu, T. Quan, L.J. Yang, L.L. Deng, X. Kang, M.J. Gao, Z.N. Xia, X. Li, D. Gao, N,Cl-codoped carbon dots from *impatiens balsamina* L. Stems and a deep eutectic solvent and their applications for gram-positive bacteria identification, antibacterial activity, cell imaging, and ClO⁻ sensing, ACS Omega 6 (2021) 29022–29036.

[34] J.P. Li, S.W. Yang, Z.Y. Liu, G. Wang, P. He, W. Wei, M.Y. Yang, Y. Deng, P. Gu, X.M. Xie, Z.H. Kang, G.Q. Ding, H.F. Zhou, X.Q. Fan, Imaging cellular aerobic glycolysis using carbon dots for early warning of tumorigenesis, Adv. Mater. 33 (2021), 2005096.

[35] S. Chen, T.T. Sun, M. Zheng, Z.G. Xie, Carbon dots based nanoscale covalent organic frameworks for photodynamic therapy, Adv. Funct. Mater. 30 (2020), 2004680.

[36] N.Q. Gong, X.W. Ma, X.H. Ye, Q.F. Zhou, X.A. Chen, X.L. Tan, S.K. Yao, S.D. Huo, T.B. Zhang, S.Z. Chen, X.C. Teng, X.X. Hu, J. Yu, Y.L. Gan, H.D. Jiang, J.H. Li, X.J. Liang, Carbon-dot-supported atomically dispersed gold as a mitochondrial oxidative stress amplifier for cancer treatment, Nat. Nanotechnol. 14 (2019) 379–387.

[37] C. Dong, S.N. Wang, M.H. Ma, P.F. Wei, Y. Chen, A.G. Wu, Z.B. Zha, H. Bi, Inhibition of oxidative stress *in vivo* through enzyme-like activity of carbon dots, Appl. Mater. Today 25 (2021), 101178.

[38] F. Li, S. Li, X.C. Guo, Y.H. Dong, C. Yao, Y.P. Liu, Y.G. Song, X.L. Tan, L.Z. Gao, D.Y. Yang, Chiral carbon dots mimicking topoisomerase I to mediate the topological

rearrangement of supercoiled DNA enantioselectively, Angew. Chem., Int. Ed. 59 (2020) 11087–11092.

[39] D. Zhou, P.T. Jing, Y. Wang, Y.C. Zhai, D. Li, Y. Xiong, A.V. Baranov, S.N. Qu, A.L. Rogach, Carbon dots produced *via* space-confined vacuum heating: maintaining efficient luminescence in both dispersed and aggregated states, Nanoscale Horiz 4 (2019) 388–395.

[40] R.B. Selvi, S. Chatterjee, D. Jagadeesan, P. Chaturbedy, B.S. Suma, M. Eswaramoorthy, T.K. Kundu, ATP driven clathrin dependent entry of carbon nanospheres prefer cells with glucose receptors, J. Nanobiotechnol. 10 (2012) 35.

[41] M. Goldberg, A.J. Smith, Cells and extracellular matrices of dentin and pulp: a biological basis for repair and tissue engineering, Crit. Rev. Oral Biol. Med. 15 (2004) 13–27.

[42] P.C. Qiu, M.B. Li, K. Chen, B. Fang, P.F. Chen, Z.B. Tang, X.F. Lin, S.W. Fan, Periosteal matrix-derived hydrogel promotes bone repair through an early immune regulation coupled with enhanced angio- and osteogenesis, Biomaterials 227 (2020), 119552.

[43] S.M. Guan, K. Zhang, J.A. Li, Recent advances in extracellular matrix for engineering stem cell responses, Curr. Med. Chem. 26 (2019) 6321–6338.

[44] F.M. Watt, W.T.S. Huck, Role of the extracellular matrix in regulating stem cell fate, Nat. Rev. Mol. Cell Biol. 14 (2013) 467–473.

[45] K. Narayanan, A. Ramachandran, J.J. Hao, G. He, K.W. Park, M. Cho, A. George, Dual functional roles of dentin matrix protein 1, J. Biol. Chem. 278 (2003) 17500–17508.

[46] M. Prasad, W.T. Butler, C.L. Qin, Dentin sialophosphoprotein in biomineralization, Connect, Tissue Res 51 (2010) 404–417.

[47] Y. Ogata, Bone sialoprotein and its transcriptional regulatory mechanism, J. Periodontal. Res. 43 (2008) 127–135.

[48] G. Chen, J.L. Chen, B. Yang, L. Li, X.Y. Luo, X.X. Zhang, L. Feng, Z.T. Jiang, M. Yu, W.H. Guo, W.D. Tian, Combination of aligned PLGA/gelatin electrospun sheets, native dental pulp extracellular matrix and treated dentin matrix as substrates for tooth root regeneration, Biomaterials 52 (2015) 56–70.

[49] F.L. Wei, C.Y. Qu, T.L. Song, G. Ding, Z.P. Fan, D.Y. Liu, Y. Liu, C.M. Zhang, S.T. Shi, S.L. Wang, Vitamin C treatment promotes mesenchymal stem cell sheet formation and tissue regeneration by elevating telomerase activity, J. Cell. Physiol. 227 (2012) 3216–3224.

[50] L. Zhou, Z.M. Liu, S.C. Chen, J. Qiu, Q.Q. Li, S.P. Wang, W. Zhou, D.Y. Chen, G. Yang, L. Guo, Transcription factor EB-mediated autophagy promotes dermal fibroblast differentiation and collagen production by regulating endoplasmic reticulum stress and autophagy-dependent secretion, Int. J. Mol. Med. 47 (2021) 547–560.

[51] J. New, S.M. Thomas, Autophagy-dependent secretion: mechanism, factors secreted, and disease implications, Autophagy 15 (2019) 1682–1693.

[52] J. New, L. Arnold, M. Ananth, S. Alvi, M. Thornton, L. Werner, O. Tawfik, H.Y. Dai, Y. Shnayder, K. Kakarala, T.T. Tsue, D.A. Girod, W.X. Ding, S. Anant, S.M. Thomas, Secretory autophagy in cancer-associated fibroblasts promotes head and neck

[53] cancer progression and offers a novel therapeutic target, Cancer Res. 77 (2017) 6679–6691.

[53] L. Cinque, A. Forrester, R. Bartolomeo, M. Svelto, R. Venditti, S. Montefusco, E. Polishchuk, E. Nusco, A. Rossi, D.L. Medina, R. Polishchuk, M.A. De Matteis, C. Settembre, FGF signalling regulates bone growth through autophagy, Nature 528 (2015) 272–275.

[54] F. Janku, T.A. Yap, F. Meric-Bernstam, Targeting the PI3K pathway in cancer: are we making headway? Nat. Rev. Clin. Oncol. 15 (2018) 273–291.

[55] L.-Y. Qin, Z.M. Ruan, R.J. Cherney, T.G.M. Dhar, J. Neels, C.A. Weigelt, J.S. Sack, A.S. Srivastava, L.A.M. Cornelius, J.A. Tino, K. Stefanski, X.M. Gu, J. Xie, V. Susulic, X.X. Yang, M. Yarde-Chinn, S. Skala, R. Bosnius, C. Goldstein, P. Davies, S. Ruepp, L. Salter-Cid, R.S. Bhide, M.A. Poss, Discovery of 7-(3-(piperazin-1-yl)phenyl) pyrrolo[2,1-f][1,2,4]triazin-4-amine derivatives as highly potent and selective PI3Kσ inhibitors, Bioorg. Med. Chem. Lett. 27 (2017) 855–861.

[56] M.S. Miller, S. Maheshwari, F.M. McRobb, K.W. Kinzler, L.M. Amzel, B. Vogelstein, S.B. Gabelli, Identification of allosteric binding sites for PI3Kα oncogenic mutant specific inhibitor design, Bioorg. Med. Chem. 25 (2017) 1481–1486.

[57] Y.L. Zhao, X. Zhang, Y.Y. Chen, S.Y. Lu, Y.F. Peng, X. Wang, C.L. Guo, A.W. Zhou, J.M. Zhang, Y. Luo, Q.C. Shen, J. Ding, L.H. Meng, J. Zhang, Crystal structures of PI3Kα complexed with PI103 and its derivatives: new directions for inhibitors design, ACS Med. Chem. Lett. 5 (2014) 138–142.

[58] L. Ai, Y.S. Yang, B.Y. Wang, J.B. Chang, Z.Y. Tang, B. Yang, S.Y. Lu, Insights into photoluminescence mechanisms of carbon dots: advances and perspectives, Sci. Bull. 66 (2021) 839–856.

[59] J.J. Liu, Y.J. Geng, D.W. Li, H. Yao, Z.P. Huo, Y.F. Li, K. Zhang, S.J. Zhu, H.T. Wei, W.Q. Xu, J.L. Jiang, B. Yang, Deep red emissive carbonized polymer dots with unprecedented narrow full width at half maximum, Adv. Mater. 32 (2020), 1906641.

[60] D.Y. Shan, J.T. Hsieh, X.C. Bai, J. Yang, Citrate-based fluorescent biomaterials, Adv. Healthcare Mater. 7 (2018), 1800532.

[61] L. Fang, X.J. Wang, M.Y. Xi, T.Q. Liu, D.L. Yin, Assessing the ligand selectivity of sphingosine kinases using molecular dynamics and mm-pbsa binding free energy calculations, Mol. Biosyst. 12 (2016) 1174–1182.

[62] S.J. Raharjo, C. Mahdi, N. Nurdiana, T. Kikuchi, F. Fatchiyah, Binding energy calculation of patchouli alcohol isomer cyclooxygenase complexes suggested as COX-1/COX-2 selective inhibitor, Adv. Bioinf. 2014 (2014), 850628.

[63] P.R. Arany, A. Cho, T.D. Hunt, G. Sidhu, K. Shin, E. Hahm, G.X. Huang, J. Weaver, A.C. Chen, B.L. Padwa, M.R. Hamblin, M.H. Barcellos-Hoff, A.B. Kulkarni, D.J. Mooney, Photoactivation of endogenous latent transforming growth factor-β1 directs dental stem cell differentiation for regeneration, Sci. Transl. Med. 6 (2014), 238ra269.

[64] A. Linde, Dentin matrix proteins: composition and possible functions in calcification, Anat. Rec. 224 (1989) 154–166.

[65] W.J. Liu, G.L. Zhang, J.R. Wu, Y.L. Zhang, J. Liu, H.Y. Luo, L.Q. Shao, Insights into the angiogenic effects of nanomaterials: mechanisms involved and potential applications, J. Nanobiotechnol. 18 (2020) 9.